Reconstruction of the Net Land Surface Energy Flux Constrained by the Energy Conservation and Land Surface Model Simulations

Ke Yang[1,2], Chunlei Liu[*1,2,3], Jiandong Li[*4], Ning Cao[1,2], Richard P. Allan[5,6], Michael Mayer[7,8], Kewei Lyu[3], Yimin Liu[4], Bian He[4], Qianye Su[1,2], Zhiting Liang[1,2], Xiaoqing Liao[9]

[1] College of Ocean and Meteorology, Guangdong Ocean University, Zhanjiang, China

[2] Laboratory for Coastal Ocean Variation and Disaster Prediction, Guangdong Ocean University, Zhanjiang, China

[3] State Key Laboratory of Marine Environmental Science, Xiamen University, Xiamen, China

[4] State Key Laboratory of Earth System Numerical Modeling and Application, Institute of Atmospheric Physics, Chinese Academy of Sciences, Beijing, China

[5] Department of Meteorology, University of Reading, Reading RG6 6BB, UK

[6] National Centre for Earth Observation, Reading, UK

[7] Department of Meteorology and Geophysics, University of Vienna, Vienna, Austria.

[8] Research Department, European Centre for Medium-Range Weather Forecasts, Bonn, Germany

[9] School of Marine Sciences, Sun Yat-sen University, Zhuhai, China

Submitted to

Advances in Atmospheric Sciences

June 2026

Corresponding author: Chunlei Liu, liuclei@gdou.edu.cn

Jiandong Li, lijd@mail.iap.ac.cn

ABSTRACT

The net land surface energy flux (F_{LS}) is a key variable controlling land–atmosphere coupling, and climate feedback mechanisms yet observational coverage is limited, and the model simulated F_{LS} values are quite spread. To address this deficiency, a novel energy conservation method is applied to CMIP6 LS3MIP (Land Surface, Snow and Soil Moisture Model Intercomparison Project) simulations to establish the relationship between the net land surface energy flux and surface temperature change at each grid point, and reconstruct gridded monthly F_{LS} from 1985-2024. Systematic validation against eddy covariance station observations demonstrates that our reconstructed F_{LS} outperforms existing products. The reconstructed F_{LS} maintains consistency with reanalyses and model simulations in terms of globally averaged anomaly variability during the common period 1985–2012, with an average correlation coefficient of 0.77. The reconstructed F_{LS} data show statistically significant correlations with observations at all stations used, a performance superior to that of reanalysis data. For turbulent fluxes derived from the reconstructed F_{LS}, approximately 71% of sites exhibit higher anomaly correlation coefficients with observations than those from reanalysis data. The high F_{LS} uncertainties are mainly distributed in Northern Hemisphere high latitudes and high-altitude zones due to large errors in snowmelt. The difference between LS3MIP and our estimation is mainly over 50-70°N, where the land area mean standard deviation (STD) from multiannual mean F_{LS} is 0.80 Wm^{-2} for LS3MIP and 0.55 Wm^{-2} for our estimation. The F_{LS} constrained by the simple energy model provide a useful reference for diagnosing land-atmosphere interactions and evaluating climate models.

Key words: net land surface energy flux; energy balance; FLUXNET observations; LS3MIP simulations

https://doi.org/10.1007/s00376-026-6191-5

Article Highlights:

- A simple energy conservation model has been built to estimate the net land surface energy flux at grid point.
- The estimated net land surface energy flux captures the interannual variability and shows good consistency with reanalyses and model data. The inferred turbulent energy fluxes show significant anomaly correlations with observations and are superior to the reanalysis datasets at 71% of the observation sites.
- Snowmelt dominates the land surface energy flux uncertainty in Northern Hemisphere high latitudes and high-altitude zones.

1. Introduction

The net surface energy flux (F_S) is a key component of energy flow in the climate system (Stephens et al., 2012, Wild et al., 2017, Liu et al., 2017, 2020), modulating the coupling processes between the surface and the atmosphere (Andrews et al., 2009; Seneviratne et al., 2010). The F_S can accumulate in the ocean and land, driving the climate change in the Earth system by altering surface temperatures (von Schuckmann et al., 2016; Hu et al., 2019). The F_S can affect the glacier melting and thereby altering the global seawater mass (Church et al., 2013; Llovel et al., 2019; Zemp et al., 2019). The F_S entering the upper ocean leads to an increase in upper ocean heat content (Levitus et al., 2012; Hakuba et al., 2024; Liu et al., 2024), resulting in the thermal expansion and sea-level rise (Church et al., 2011). If F_S accumulates in the top layer of the soil, land temperatures will rise rapidly due to the much lower effective heat capacity of soil compared to the ocean, as the land cannot circulate freely like the ocean (Cuesta-Valero et al., 2021, 2025; Wang et al., 2024). This thermodynamic response can drive and exacerbate the frequency and intensity of extreme heat events (Huntingford et al., 2024; Tian et al., 2024). Moreover, the excessive accumulation of energy in land can reduce the temperate vegetation productivity (Ciais et al., 2005; Seneviratne et al., 2006; Heimann and Reichstein, 2008) and disrupt the net CO_2 exchange in the temperate land-atmosphere system, turning temperate ecosystems from carbon sinks into sources. Considering the multi-scale regulatory role of the F_S in the climate system, it is essential to quantify the F_S precisely in order to understand global climate change and its feedback mechanisms.

The F_S in reanalysis and climate model simulations is derived from the radiative transfer models and empirical bulk formula, leading to substantial uncertainties (Macdonald and Baringer, 2013; Josey et al., 2013; Valdivieso et al., 2017) due to the deficiencies in models and data assimilation systems (Liu et al., 2017). In CMIP6 model simulations, the global average F_S for 2001–2010 ranged from 0.8 to 2.0 Wm^{-2} (Wild, 2020). The multi-model mean F_S for 2000–2009 was 1.6 Wm^{-2}, exceeding the multi-model mean net energy imbalance at the top of the atmosphere 1.3 Wm^{-2} (Li et al., 2023). This indicates a widespread energy conservation issue in the model simulations. For the reanalysis products, Wild and Bosilovich (2024) showed that the global mean F_S across ten datasets spans from –11 to 11 Wm^{-2}, with a standard deviation of 6.4 Wm^{-2}, far greater than the corresponding value of 0.3 Wm^{-2} from CMIP6 models. Further analysis by Mayer et al. (2024) confirmed this wide spread of F_S in reanalyses. They also decomposed the F_S into the global ocean and land area means, showing that 4 out of nine reanalyses have an unrealistic global land area mean F_S greater than 1 Wm^{-2}, with the maximum of 8.1 Wm^{-2}.

It is known that the mass balance in the atmospheric reanalysis is not maintained due to the simultaneous assimilation of the wind field and surface pressure (Trenberth et al., 2009; Mayer and Haimberger, 2012; Liu et al., 2015), so the energy conservation is not satisfied and ultimately results in large biases in Fs. In order to solve this problem, a residual method has been developed to estimate the net surface energy flux F_S. It combines the TOA (top of the atmosphere) radiative energy fluxes, the atmospheric energy divergence and the total atmospheric energy tendency from atmospheric reanalysis to estimate the F_S (Trenberth et al., 1994, 2001, 2009; Chiodo and Haimberger, 2010; Mayer and Haimberger, 2012; Liu et al., 2015; Loeb et al., 2022; Mayer et al., 2024), where both the atmospheric energy divergence and the total atmospheric energy tendency are mass corrected. Therefore, it ensures the mass and energy conservation and is superior to other methods (Trenberth et al., 2001; Cheng et al., 2019). Mayer et al. (2024) analysed F_S from three datasets estimated from the residual method applied to ERA5, MERRA2 and JRA55, and they found that although the global area mean F_S is reasonable, the global land area mean net surface energy flux of 5.4 Wm^{-2} from JRA55 is not physically realistic. Furthermore, the meridional heat transport inferred from the ocean surface flux derived from the residual method is also systematically lower than observations (Trenberth et al., 2019).

The problem in the F_S estimated from the residual method has also been noticed by Liu et al. (2015, 2017), so the net land surface energy flux (F_{LS}) has been adjusted by constraining the global land area mean F_{LS} based on observations. The observation-based estimation of F_S by Liu et al. (2015, 2017, 2020, 2022) using the residual method and land adjustment has been used widely in the climate research and model valuations (Williams et al., 2015; Senior et al., 2016; Trenberth and Fasullo, 2017; Mayer et al., 2022; Ren and Zhou, 2024). The generated product, including the F_S and total column atmospheric energy divergence, together with the TOA radiative energy fluxes (Allan et al., 2014; Liu et al., 2015, 2017, 2020, 2022; Mayer et al., 2017, 2021), has been referenced as the DEEPC (Diagnosing Earth's Energy Pathways in the Climate system) dataset. Evaluations of the DEEPC F_S have been mostly focused on the ocean surface (Meyssignac et al., 2019; Liu et al., 2022; Hakuba et al., 2021; Liu et al., 2022; Mayer et al., 2022). The inferred northward meridional ocean heat transport at 26°N in the Atlantic from DEEPC dataset has been compared with the RAPID (Rapid Climate

Change‑Meridional Overturning Circulation and Heatflux Array) observations, and there is good agreement between both magnitude and variability. This validation indirectly shows the reliability of the method in estimating sea surface energy fluxes (Liu et al., 2022). However, the net land surface energy flux F_{LS} has not been properly validated so far due to the sparse of observations. Although the changes in F_{LS} have small effect on the F_S over the ocean due to the small mean amplitude of F_{LS} compared with that over the ocean, it is still essential to have the accurate F_{LS}, since many regional phenomena are sensitive to the F_{LS}, such as the Boreal Summer Intraseasonal Oscillation (Goswami and Shukla, 1984; Kikuchi, 2021). This study employs a physically constrained framework that, unlike traditional statistical or empirical methods, effectively ensures the physical consistency. The main object of this study is to (1) identify a physically meaningful relationship between the surface temperature change and the net surface energy flux over land, in order to build the realistic net land surface energy flux; (2) compare the derived net land surface energy fluxes with FLUXNET observations (Pastorello et al., 2020) to evaluate the estimation.

2. Data and Methods

2.1. *Data sets*

2.1.1 *Simulated land surface energy fluxes*

The simulated land surface energy fluxes from the LS3MIP (Land Surface, Snow and Soil Moisture Model Intercomparison Project) model simulations over 1985-2012 have been employed in this study to investigate the relationship between the land surface temperature variation and F_{LS}. As a newly introduced component of CMIP6, LS3MIP employed land surface models specifically designed to comprehensively evaluate climate feedback mechanisms associated with land surface processes, particularly snow cover and soil moisture (Van Den Hurk et al., 2016). These models focused on detailed parameterization of terrestrial processes, especially the climatic impacts of snowpack, soil moisture, and land surface energy fluxes. The model configuration incorporates soil conditions and land surface states, accounts for snow shortwave radiation effects, and particularly emphasizes two key land-atmosphere feedbacks: the snow-albedo-temperature feedback involved in Arctic amplification, and the soil moisture-temperature feedback contributing to extreme temperature events (Douville et al., 2016).

Due to the limited number of models currently released under LS3MIP and the lack of surface energy flux-related variables in some models, four models having complete output variables with three historical scenarios (Land-Hist-princeton, Land-Hist-cruNcep, and Land-Hist-wfdei) have been selected in this study. Land-Hist-princeton indicates the use of atmospheric forcing data from Princeton (Sheffield et al., 2006), the Land-Hist-cruNcep uses the CRU-NCEP forcing dataset (Viovy and Ciais, 2009), and the Land-Hist-wfdei uses the combined WFD (WATCH Forcing Data) and WFDEI (WATCH Forcing Data methodology applied to ERA-Interim data) forcing data (Weedon et al., 2011), where WATCH is the EU Water and Global Change project including simulation of the global terrestrial water cycle in the twentieth century via a suite of hydrological models and model intercomparison (Harding et al., 2011). WATCH forcing data is based on the ECMWF ERA-40 reanalysis and includes elevation correction and monthly bias correction using CRU (Climate Research Unit) observations. ERA40 and ERA-Interim data are used by WFD / WFDEI, and NCEP reanalysis data are used by Princeton. The used variables include the temperature at 2m, precipitation, radiative fluxes and surface pressure, etc. These scenarios differ only in their forcing datasets while maintaining identical model configurations. To facilitate inter-model comparison and F_{LS} data reconstruction, bilinear interpolation has been applied to standardize all model outputs to a uniform horizontal resolution of 0.25°×0.25°.

2.1.2 *Land surface energy fluxes from atmospheric reanalysis*

To assess the uncertainties of our reconstructed F_{LS} and validate its consistency, land surface energy fluxes from two atmospheric reanalyses, ERA5 and MERRA2, are also used in this study. The ERA5 atmospheric reanalysis is developed by the ECMWF (European Centre for Medium-Range Weather Forecasts). It assimilates extensive satellite and in-situ observations into numerical weather prediction model, providing high-resolution meteorological data from 1940 to present at a horizontal resolution of 0.25°×0.25°. The MERRA2 (The Modern-Era Retrospective Analysis for Research and Applications, Version 2) is the atmospheric reanalysis product developed by NASA's Global Modeling and Assimilation Office (GMAO). MERRA2 utilizes the Goddard Earth Observing System Model Version 5 (GEOS-5) and assimilates multiple types of observational data and satellite measurements. Both reanalysis datasets provide comprehensive global meteorological data and have been widely used by the community. Additionally, the data from ERA5-Land are also included for a comprehensive comparison (Muñoz-Sabater et al. 2021). ERA5-Land employs the same land surface model as ERA5 but without data assimilation. The land surface F_{LS} from DEEPC (Diagnosing Earth's Energy Pathways in the Climate System) version 5 dataset developed by Liu and Allan (2022) is also used for comparison and consistency check.

2.1.3 *FLUXNET observations*

To validate the estimated net land surface flux F_{LS}, in-situ observations (FLUXNET) from flux towers over 1997-2014 were utilized. The FLUXNET provides globally distributed eddy covariance measurements of biosphere-atmosphere exchanges of water and energy fluxes, including the shortwave and longwave fluxes, and sensible and latent heat fluxes, along with ancillary meteorological variables, from 212 terrestrial sites worldwide (Pastorello et al., 2020). These observations have undergone standardized quality control and processing protocols, and have been widely employed for land surface process applications and model evaluations (Fisher et al., 2008; Zhang et al., 2017; Gerken et al., 2019). Due to missing measurements and quality control issues for the selected variables at the sites, the data from sites with more than three years of continuous observations and good quality control have been selected for comparison in order to ensure its validity. A total of 60 sites have been selected, among which 39 sites with complete surface energy flux data were used to validate F_{LS}. The site locations are marked in Figure S1 and they are mainly concentrated in the United States and Europe, the relevant sites information is listed in Table S1, and the frequency of the station having different data length (months) is displayed in Figure S2 for reference.

The surface radiative energy fluxes were obtained from the CERES-EABF (Clouds and the Earth's Radiant Energy System Energy-Balanced and Filled) Edition 4.2. The CERES-EABF provides the global TOA and surface radiative fluxes from March 2000 onwards. This dataset is primarily based on satellite observations and has been demonstrated to be of high quality, being widely used in climate change researches. All aforementioned datasets with brief descriptions are listed in Table 1.

Table 1. Datasets and brief descriptions

Data set	Forcing data set	Period (in this study)	Resolution	References
FLUXNET		1997-2014	station	*Pastorello et al.* (2020)
ERA5		1980-2024	0.25°×0.25°	*Hersbach et al.* (2020)
ERA5-Land		1980-2024	0.1°×0.1°	*Muñoz-Sabater et al.* (2021)

MERRA2		1980-2024	0.5°×0.625°	*Gelaro et al*. (2017)
DEEPCv5		1985-2017	0.7°×0.7°	*Liu and Allan* (2022)
CERES-EABF Ed 4.2		2001-2024	1°×1°	*Loeb et al.* (2018); *Kato et al.* (2018)
LS3MIP		1979-2012		
CNRM-CM6-1	Princeton		1.4°×1.4°	*Voldoire et al.* (2019)
	WFDEI		1.4°×1.4°	
CNRM-ESM2-1	Princeton		1.4°×1.4°	*Séférian et al.* (2019)
	CRU-NCEP		1.4°×1.4°	
E3SM-1-1	Princeton		0.5°×0.5°	*Burrows et al.* (2020)
	CRU-NCEP		0.5°×0.5°	
IPSL-CM6A-LR	CRU-NCEP		1.27°×2.5°	*Boucher et al.* (2020)

2.2 *Net land surface energy flux reconstruction*

Although the models directly solve the heat transfer equation, the simulated F_{LS} is still quite spread due to different complicated parameterizations (Figure S3). Following Liu et al. (2015, 2017), the reconstruction of the F_{LS} is based on the energy balance algorithm. The relationship between the F_{LS} and surface temperature change ($\frac{\Delta T_{LS}}{\Delta t}$) is built and can be written as:

$$F_{LS} - F_{snow} = C\frac{\Delta T_{LS}}{\Delta t} + \varepsilon \tag{1}$$

where F_{snow} is the energy required for snow melt, C is the effective heat capacity depending on the characteristics of the soil canopy and the moisture content within the soil (Boer et al., 1993; Schwartz, 2007), and ε represents the residual energy penetrating to the deep soil. T_{LS} is the land surface temperature and t is the time. $\frac{\Delta T_{LS}}{\Delta t}$ is calculated based on consecutive monthly skin temperature values, for instance, the $\frac{\Delta T_{LS}}{\Delta t}$ for February can be computed based on the difference between February and January, and so on. C and ε are obtained by applying Equation (1) to the LS3MIP model data. Considering the significant uncertainties in the F_{snow} simulations across grid point by the LS3MIP models, (C, ε) are computed with and without F_{snow} at a grid point, therefore 14 pairs of (C, ε) values are obtained for each grid point in each month from January-December. Two methods have been employed for the F_{LS} reconstruction: (1) the pair of (C, ε) is selected with the higher positive correlation between $F_{LS} - F_{snow}$ (or F_{LS}) and $\frac{\Delta T_{LS}}{\Delta t}$ with and without the consideration of F_{snow}, therefore seven sets of (C, ε) values can be obtained, and seven F_{LS} datasets can be estimated, the mean F_{LS} can be regarded as the reconstruction and noted as F_{LS1}; (2) (C, ε) can also be selected with the highest positive correlation between $F_{LS} - F_{snow}$ (or F_{LS}) and $\frac{\Delta T_{LS}}{\Delta t}$ from fourteen (C, ε) pairs at a grid point (seven sets with F_{snow} consideration and seven sets without). Because the large uncertainties in the F_{snow} simulations, the relationship can be better at a grid point with the consideration of F_{snow}, but also possibly worse at another grid point due to the unrealistic F_{snow} as shown in Figure S4. Then one F_{LS} dataset can be reconstructed based on the best selected (C, ε) and noted as F_{LS2}.

This method effectively reduces the uncertainty impact in the F_{snow} simulations. The selected optimal (C, ε) can be applied to the observed land surface temperature (T_{LS}) and snow melt F_{snow} data to reconstruct $F_{LS.}$ Since F_{snow} is a variable that cannot be directly observed and must be derived through model estimation, the F_{snow} from ERA5 are used in this study, since ERA5 assimilated observational data from 4,689 stations worldwide, including snow depth and snow cover, ensuring relatively high accuracy (Urraca and Gobron, 2023). Furthermore, the global mean F_{LS} reconstruction for the period 2004–2014 is anchored at 0.2 Wm^{-2} (Gentine et al., 2019). The improvement of this method is the optimal selection of (C, ε) from a group of the state-of-the-art land surface model output, to ensure the rationality of the physical relationship at the grid point.

When comparing reanalysis and reconstructed F_{LS} with FLUXNET observations, the four grid points closest to the observation station are selected and the data are bilinearly interpolated to the station point. The evaluation metrics selected are Bias and Mean Absolute Error (MAE), which are defined as follows:

$$Bias = \frac{\sum_{i=1}^{N} (X_i - O_i)}{N} \tag{2}$$

$$MAE = \frac{\sum_{i=1}^{N} |X_i - O_i|}{N} \tag{3}$$

where N is the total number of samples, X_i and O_i are the comparative and observational values, respectively. Compared with the commonly used RMSE (Root Mean Square Error), the MAE can reduce the large impact of the outliers.

Unless specified, the two-tailed t-test will be used for the significance test of the Pearson correlation coefficient (Hipel and Mcleod, 1994), the Mann–Kendall test is used to check the significance of the trend, and the significance level is defined as 95%. The downward direction is defined as the positive direction for all energy fluxes.

3. Results

3.1 *Comparison of net land surface energy fluxes*

The anomaly time series of the net land surface energy fluxes from the reconstructed F_{LS1}, LS3MIP models, ERA5, ERA5-Land and MERRA2 are plotted in Figure 1. The anomalies are computed relative to the reference period 1990-2010, and all lines are six month running means. The F_{LS1} shows good consistency with other datasets in terms of interannual variability during the common period 1985-2012, and the correlation coefficients between F_{LS1} and ERA5, ERA5-Land, MERRA2, LS3MIP and DEEPCv5 are 0.65, 0.73, 0.72, 0.84, and 0.89, respectively, with an average correlation coefficient of 0.77. All these correlation coefficients are statistically significant at the 95% confidence level. However, it is noticed that there is an unrealistic big jump (reaching 5.68 Wm^{-2}) of the ERA5-Land anomaly over 2023-2024, and the MERRA2 anomalies are spiky after 2006, indicating a climatology shift of the MERRA2 F_{LS} as shown in Figure S5a, the spike range agrees with the climatology differences (Figure S5b). The F_{LS1} can capture the cooling events, such as the

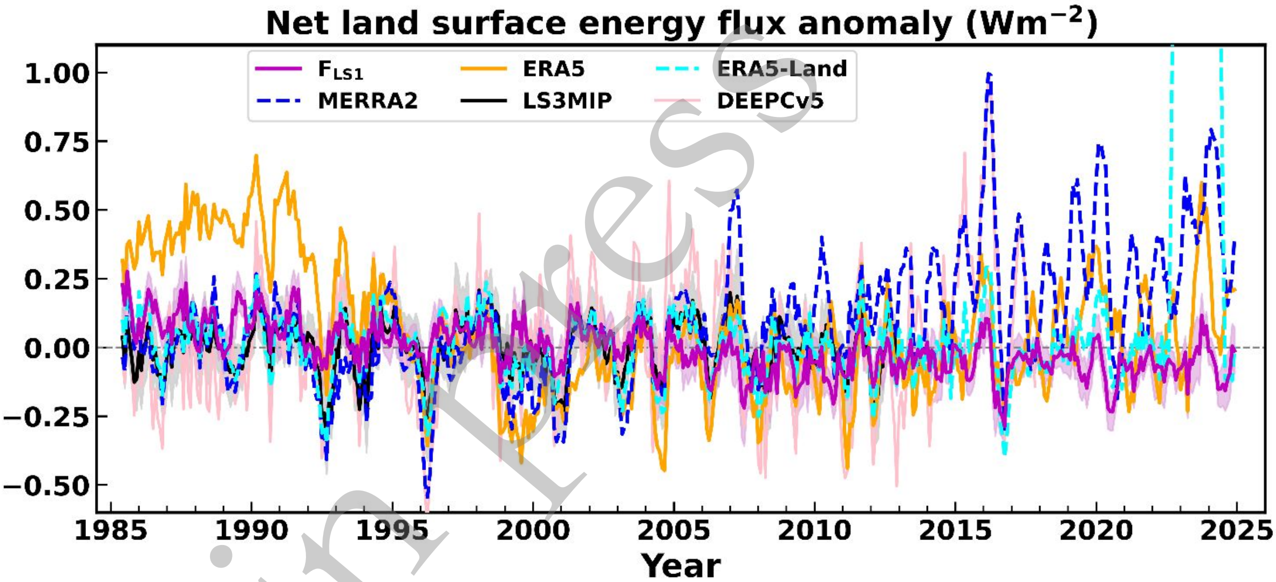

Figure 1. Monthly anomaly time series of the net land surface energy flux, with reference period from 1990–2010. All lines are 6 month running means. The solid black and purple lines are ensemble means and the corresponding light shades are the mean ± one standard deviation from seven datasets, respectively.

temperature decline caused by the 1991 Mount Pinatubo volcanic eruption and the 1996 La Niña event (WMO 1997; Schwing et al., 2002; Hersbach et al., 2020), but the reproduced amplitude is relatively small. The F_{LS} from ERA5 has much higher anomaly over 1985 to 1992 than other datasets, and it decreases rapidly after 1991, due to changes in the observing system (Hersbach et al., 2020). The F_{LS1}

and F_{LS2} are nearly identical (***r*** = 0.99), so only F_{LS1} is considered in the following analysis.

The means and trends of F_{LS} over different time periods are listed in Table 2. The F_{LS1} and ERA5 time series show significant downward trends at the 95% confidence level during both 1985–2012 (-0.07±0.02 and -0.22±0.03 $Wm^{-2}(10yr)^{-1}$) and 1985–2024 (-0.04±0.01 and -0.08±0.02 $Wm^{-2}(10yr)^{-1}$), whereas MERRA2 exhibits a significant upward trend (0.05±0.02 $Wm^{-2}(10yr)^{-1}$ over 1985–2012 and 0.11±0.02 $Wm^{-2}(10yr)^{-1}$ over 1985–2024), and the trends from the LS3MIP simulations are not significant. The spatial distribution of F_{LS} trends over 1985–2024 exhibits considerable differences among different datasets. However, consistent increasing trends are observed across all datasets over Greenland, the western Tibetan Plateau and Australia (Figure S6). The mean F_{LS} values from all datasets are positive, indicating the accumulation of the energy in the soil throughout the study period. It is noticed that F_{LS} values from other datasets are much larger than that of the reconstructed F_{LS1}.

Table 2. Mean and trend of the global land area mean F_{LS}. Significant trends are in bold (p < 0.05).

Trend ($Wm^{-2}(10yr)^{-1}$)	F_{LS1}	ERA5	ERA5-Land	MERRA2	LS3MIP
1985-2012	**-0.07±0.02**	**-0.22±0.03**	-0.03±0.02	**0.05±0.02**	0.00±0.02
2010-2015	0.10±0.16	0.30±0.26	0.14±0.25	0.45±0.25	
2013-2024	-0.02±0.05	**0.17±0.09**	**1.76±0.32**	0.16±0.10	
1985-2024	**-0.04±0.01**	**-0.08±0.02**	**0.18±0.03**	**0.11±0.02**	
Mean (Wm^{-2})	F_{LS1}	ERA5	ERA5-Land	MERRA2	LS3MIP
1985-2012	0.27	0.74	0.83	0.78	0.46
2013-2024	0.21	0.72	1.29	1.07	
1985-2024	0.25	0.74	0.96	0.87	

To assess the robustness of the declining F_{LS1} trend from 1985-2012, the time series of the global land area mean surface temperature T_{LS} trend from successive 60 months are calculated and plotted in Figure 2. All datasets show overall significant downward tendency (p<0.05) over 1985-2012, indicating a sustained deceleration in the rate of surface warming, consistent with the declining trend of F_{LS1}.

The downward trend of ERA5 F_{LS} from 1985-2012 is partly due to the excessively high positive anomalies before 1995 and therefore questionable (Figure 1). In order to further investigate the reasons of the downward F_{LS1} trend, the ΔT_{LS} and F_{snow} time series from ERA5 are plotted in Figures 3a and b, respectively. The trends for ΔT_{LS} from reanalyses over 1985-2012 and 1985-2024 are insignificant, while the downward trends of F_{snow} over these two periods are –0.08±0.01 Wm^{-2} $(10yr)^{-1}$ and –0.05±0.01 Wm^{-2} $(10yr)^{-1}$, respectively, which are statistically significant and therefore dominates the F_{LS1} trend based on Equation (1). The snow data from thousands of stations have been assimilated to the ERA5 system, yielding consistent results with independent observations (Mortimer et al., 2024, Majidi et al., 2025). However, the snow product is susceptible to changes in the assimilation system (Winkelbauer et al., 2022). For instance, in 2004, ERA5 began assimilating the Interactive Multisensor Snow and Ice Mapping System (IMS) product from the National Oceanic and Atmospheric Administration (NOAA). While this notably improved the estimation accuracy, it also introduced a discontinuity in the time series (Kouki et al., 2023, Urraca and Gobron, 2023). This discontinuity has implications for the long-term trend analysis derived from the reconstructed data. Considering the large discrepancies between F_{snow} data from different datasets (Figure S7), their effects on the F_{LS} merit further investigation.

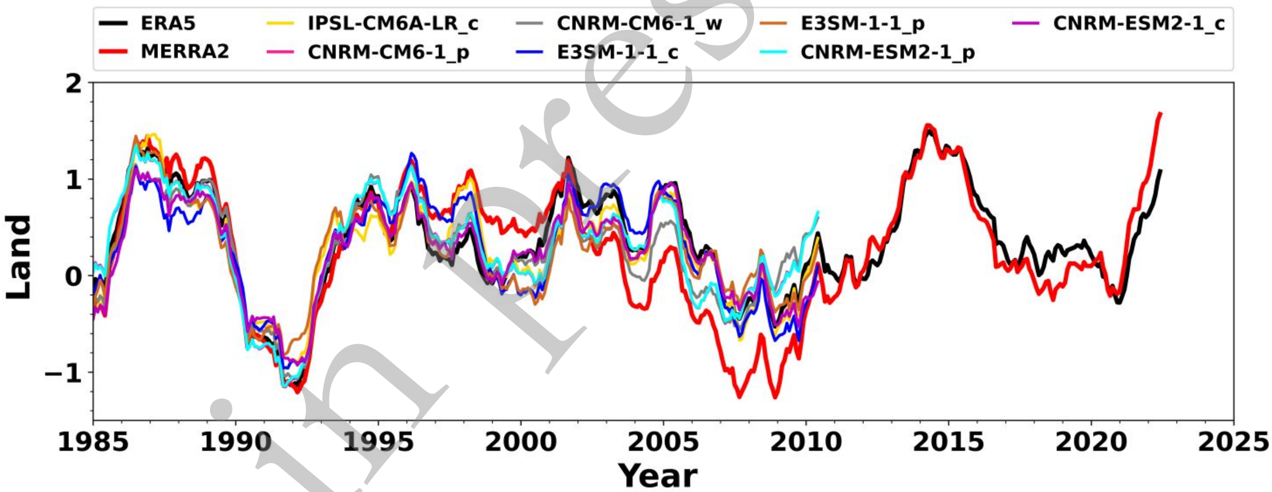

Figure 2. Time series of the global land area mean T_{LS} trend calculated for successive 60 months and different datasets. The unit is $K(10yr)^{-1}$.

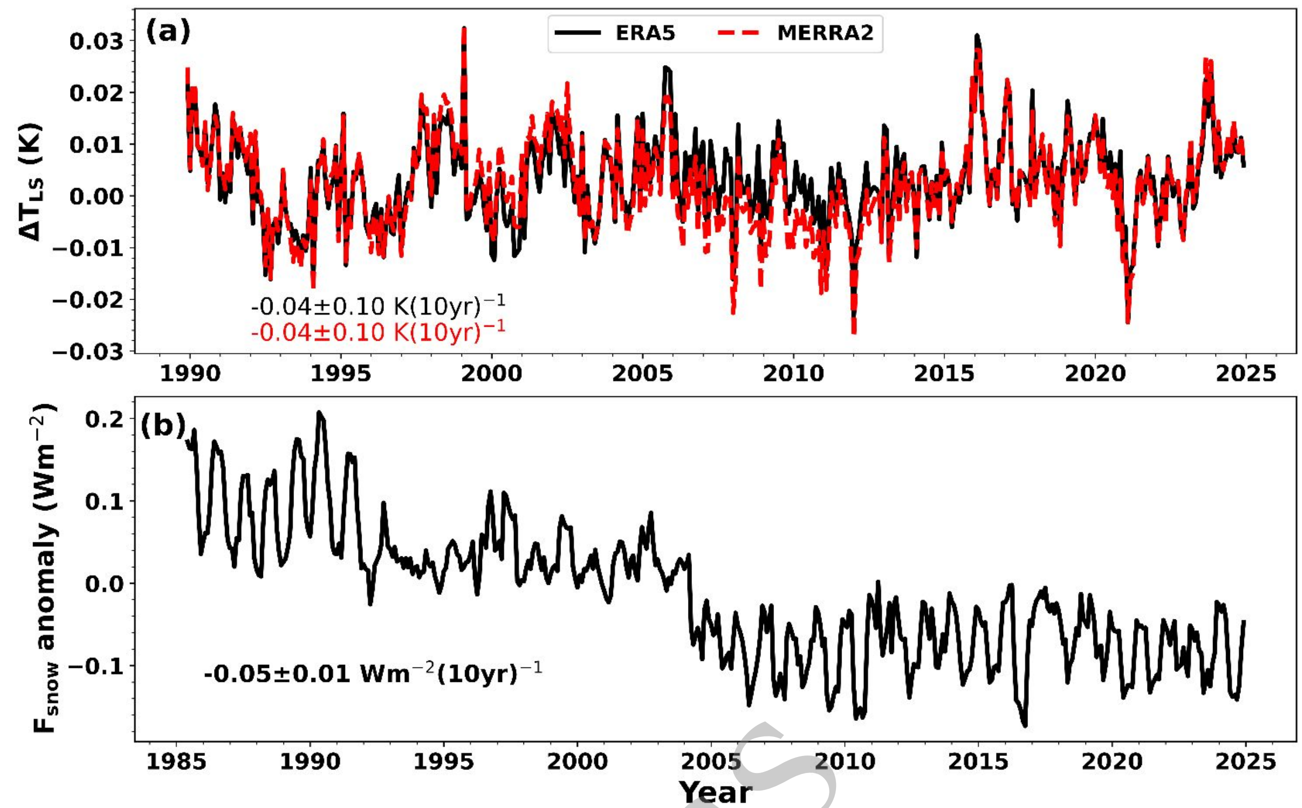

Figure 3. Time series over 1985-2024. (a) The change of global land area mean surface temperature (ΔT_{LS}) smoothed by 60 month running mean, (b) the anomaly of energy required for snow melt smoothed by 6 month running mean. The trends over 1985-2024 are also displayed.

3.2 *Compared with FLUXNET observations*

3.2.1 *Net land surface energy flux*

The observational data of the net surface energy fluxes over land remain scarce, and the FLUXNET observations are commonly used for evaluations of the land surface energy fluxes (Fisher et al., 2008; Muñoz-Sabater et al., 2021; Xu et al., 2023). The Bias, MAE and the correlation coefficient (***r***) between FLUXNET observations and other datasets (F_{LS1}, DEEPCv5, ERA5, ERA5-Land and MERRA2) are calculated over 1985-2012 for data from each station using total values (not anomaly) first, and they are then displayed as the box plot as shown in Figure 4.

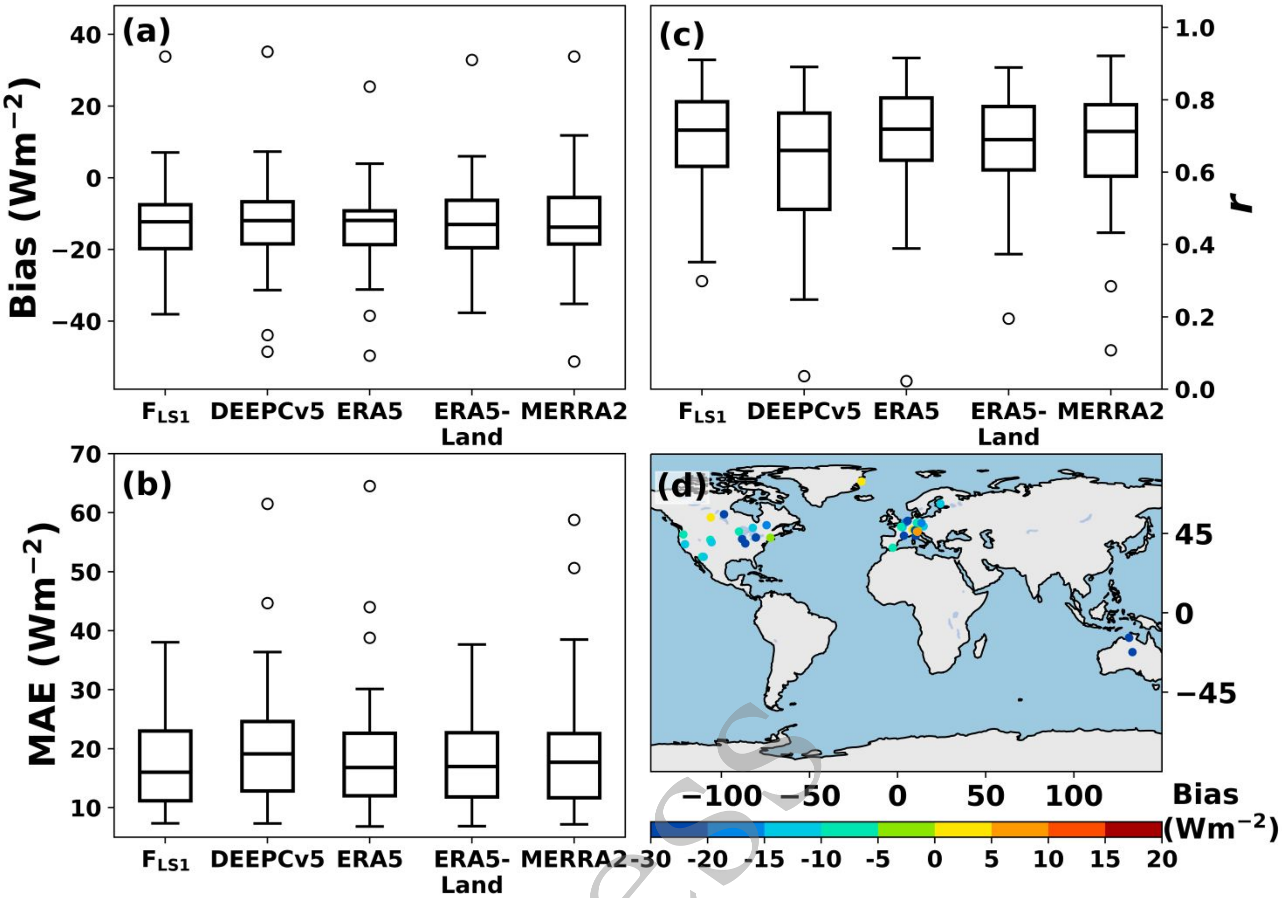

Figure 4. Box plots showing the evaluation of monthly net surface energy fluxes from F_{LS1}, DEEPCv5, ERA5, ERA5-Land and MERRA2 against the in situ FLUXNET observations. Statistics include the (a) Bias, (b) MAE, and (c) correlation coefficient (***r***). The central mark in the box indicates the median, the bottom and top edges of the box indicate the 25th and 75th percentiles. Hollow circles are considered outliers. (d) Geographical distribution of F_{LS1} bias in land surface net energy flux across 39 observation sites.

The negative biases indicate the systematic underestimation of F_{LS} from all five datasets relative to observations (downward is defined as the positive direction) (Figure 4a). The MAE medians are 16.0, 19.1, 16.9, 17.0 and 17.7 Wm^{-2} for F_{LS1}, DEEPCv5, ERA5, ERA5-Land and MERRA2, respectively, so the F_{LS1} performs only marginally better than other four datasets (Figure 4b). Both biases and MAEs are so large that the measurements are sceptical for their systematic errors. For the correlation coefficient (***r***) (Figure 4c), F_{LS1} and ERA5 have the same median value of 0.72, and both of them outperform DEEPCv5 (***r*** = 0.66), ERA5-Land (***r*** = 0.69) and MERRA2 (***r*** = 0.71). It is noticed that F_{LS1} data and FLUXNET observations have statistically significant correlations at all stations ($p<0.05$), a performance superior to other datasets. Since the time series for F_{LS} is short at most stations, data from 39 selected stations are also composited to form a long series for the calculation of the correlation coefficient, and the $\boldsymbol{r} = 0.49$ (Figure S8), 0.29, 0.46, 0.48 and 0.39 between FLUXNET and F_{LS1}, DEEPCv5, ERA5, ERA5-Land and MERRA2, respectively. The F_{LS1} data are still the closest to the observations.

Due to the limited number and distribution of observation sites, the validation of F_{LS} in this study primarily relies on the data from North America and Europe, supplemented by a few sites in Greenland and Australia (Figure 4d). Results show that the F_{LS1} exhibit negative biases at the vast majority of sites in North America, Europe, and Australia, while positive biases are observed at the sites in Greenland. It should be noted that the observations are generally affected by the energy non-closure issue (Wilson et al., 2002), therefore the calculated biases may stem partly from systematic errors in the observations.

3.2.2 *Land surface turbulent energy flux*

As a key component of the surface energy flux, the surface turbulent flux plays an important role in both the water and energy cycles. ERA5, ERA5-Land and MERRA2 have the surface turbulent flux output. The land surface turbulent fluxes from DEEPCv5 and our estimation are obtained by subtracting the CERES-EBAF surface radiative flux from the net surface energy flux F_{LS}.

The CERES surface radiative fluxes (shortwave + longwave) are also compared with the FLUXNET observations as shown in Figure 5. The results from the composite series show that both the seasonal variations and anomaly sequences are consistent between two datasets, with the correlation coefficients of 0.96 (Figure 5a) and 0.62 (Figure 5b), respectively. Although the surface radiative fluxes from CERES are derived through inference rather than direct measurement of surface fluxes, the consistency between CERES surface radiative fluxes and FLUXNET data indicates the reliability of CERES observations, thereby supporting our estimation of turbulent fluxes.

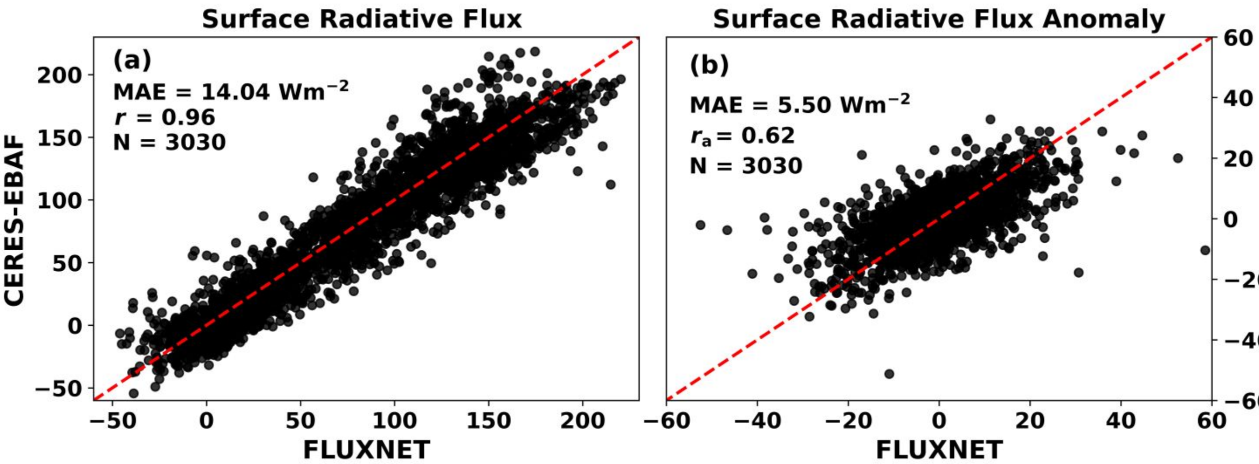

Figure 5. The scatter plot between radiative fluxes (shortwave + longwave) from the CERES-EBAF and FLUXNET. (a) Surface radiative flux, (b) surface radiative flux anomaly. The dashed red line is the symmetrical line y=x.

The turbulent fluxes were evaluated for the period 2001–2014, with the results shown in Figure 6. Similarly to Figure 4a, the median biases are all negative, implying the overestimation of the turbulent fluxes by four datasets compared with the FLUXNET observations considering that the surface turbulent flux flow is actually from land to the atmosphere. This may partly contribute from the observations since the eddy covariance method often underestimates the turbulent fluxes (Wilson et al., 2002; Mauder et al., 2024). The median biases are -11.5, -11.0, -6.8, -4.74 and -15.3 Wm^{-2} for F_{LS1}, DEEPCv5, ERA5, ERA5-Land and MERRA2, respectively, so the ERA5-Land has the best performance regarding to the median bias (Figure 6a). The corresponding median MAE values are 21.06, 21.18, 20.76, 18.58 and 25.08 Wm^{-2}, respectively (Figure 6b). The median anomaly correlation coefficients are 0.41, 0.33, 0.35, 0.40 and 0.33 for F_{LS1}, DEEPCv5, ERA5, ERA5-Land and MERRA2, respectively (Figure 6c). They are statistically significant but relatively small. The anomaly correlation coefficient from F_{LS1} is higher than other datasets at approximately 71% of the sites, with about 9.1% of the sites showing significantly higher values compared to other datasets (z-test, $p < 0.05$). The corresponding median correlation coefficients can be 0.93, 0.90, 0.92, 0.93 and 0.91 if the total surface turbulent fluxes are employed due to the seasonal cycle.

Figure 6d shows a scatter plot comparing our estimated surface turbulent fluxes against FLUXNET observations composited from all 60 selected stations (total data points N = 6963). The correlation coefficients are ***r*** =0.86 (Figure 6d), 0.72, 0.83, 0.85 and 0.81 for F_{LS1}, DEEPCv5, ERA5, ERA5-Land and MERRA2, respectively. The correlation coefficient of F_{LS1} is significantly higher than other datasets at the 95% confidence level, indicating that these datasets can capture the observed variations and the estimated surface turbulent fluxes from F_{LS1} performs slightly better than other datasets.

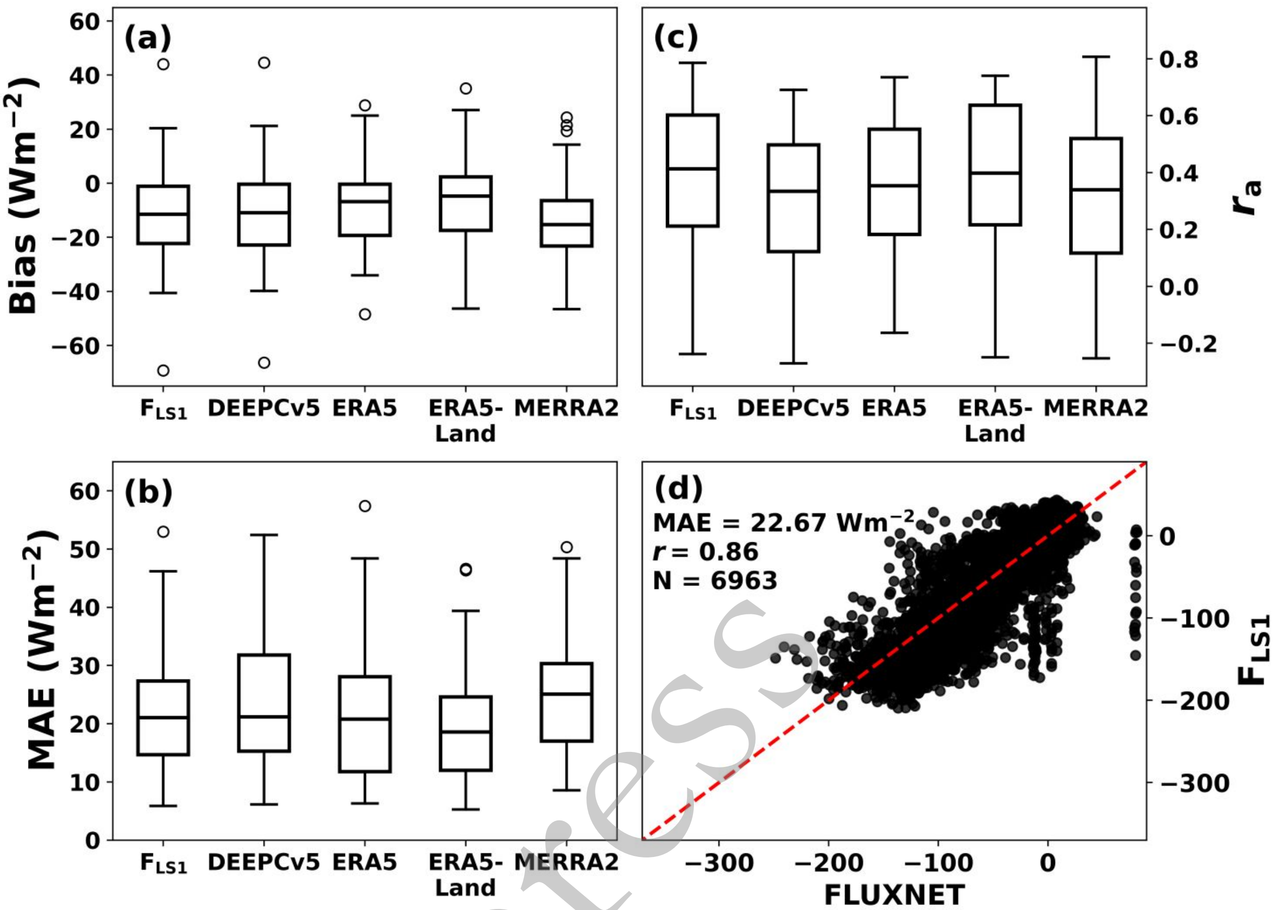

Figure 6. Box plots showing the evaluation of surface turbulent fluxes from F_{LS1}, DEEPCv5, ERA5, ERA5-Land and MERRA2 against the in situ FLUXNET observations. Statistics include the (a) Bias, (b) MAE, and (c) anomaly correlation coefficient ($\boldsymbol{r_a}$). The central mark in the box indicates the median, the bottom and top edges of the box indicate the 25th and 75th percentiles. Hollow circles are outliers. (d) is the scatter plot of surface turbulent fluxes between our estimation (F_{LS1}-CERES radiative flux) and FLUXNET, the dashed red line is the symmetrical line y=x, and N is the total number of data points.

3.3 *Uncertainties of land surface net energy flux*

In order to investigate the spatial distribution of the land surface energy flux uncertainty in both model simulations and reconstructions, the standard deviation (STD) of the multiannual mean land surface net energy flux over 1985-2012 from the seven LS3MIP simulations and seven estimations are plotted in Figure 7. Both datasets show that the large discrepancies occur in mid-to-high latitude along the land-sea boundary regions, as well as over the elevated areas such as the Rocky mountains, Iceland

and the Tibetan Plateau. The global land area mean STD is 0.34 Wm^{-2} from seven LS3MIP

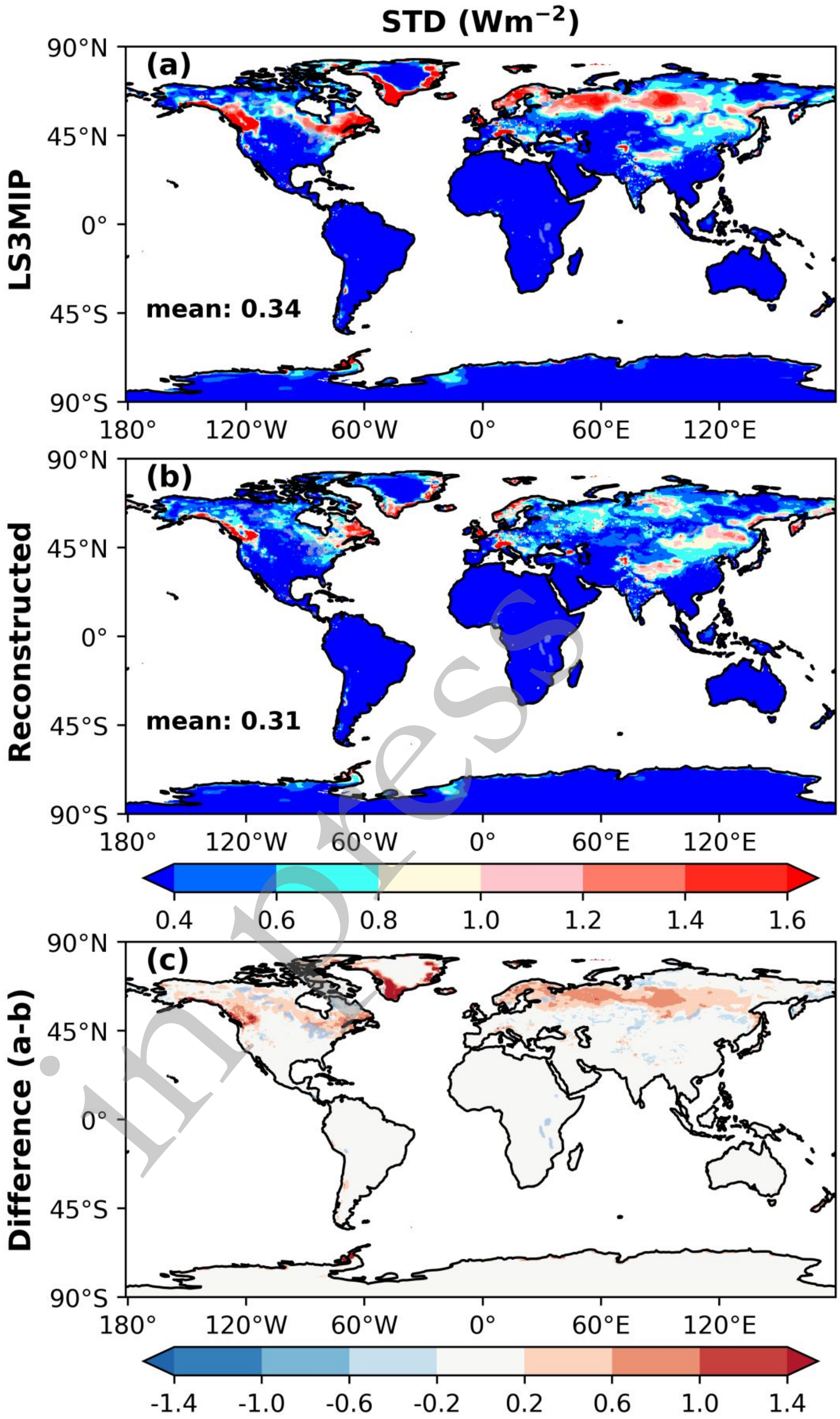

Figure 7. Spatial distribution of the land surface net energy flux standard deviations (STD) over 1985–2012 for (a) LS3MIP model simulations and (b) reconstructed F_{LS1}. (c) is the difference between (a) and (b).

simulations (Figure 7a) and 0.31 Wm^{-2} from our estimations (Figure 7b). The overall STD between 50-70°N is reduced from 0.80 Wm^{-2} for LS3MIP to 0.55 Wm^{-2} for our estimation, and this reduction is mainly concentrated in the spring snowmelt period (March–May) (Figure S9). The large STD distribution pattern may stem from the radiation budget calculation errors over complex terrain areas, due to large uncertainties introduced by the seasonal snow cover (Robledano et al., 2022). STD is also computed using the monthly data and then averaged at each grid point, and the results show similar features with Figure 7. Of course, the uncertainty estimation presented here is only from one perspective and incomplete.

4. Discussion and conclusions

Trained on CMIP6 LS3MIP land surface climate model simulations and applied to reanalysis land surface temperature changes, an energy constrained estimate of net land surface energy flux F_{LS1} has been derived using an energy balance model from Liu et al. (2017). The F_{LS1} data have been estimated via the optimised relationship between the grid-scale net surface energy flux and temperature change, in order to provide an improved, independent observation-based dataset for the climate change community.

The reconstructed net land surface energy flux F_{LS1} shows a mean anomaly correlation coefficient of 0.84 with the model simulations and consistent variability with reanalysis data of ERA5, ERA5-Land and MERRA2 (Figure 1). The F_{LS1} shows a significant decreasing trend (–0.07± 0.02 W m^{-2} $(10yr)^{-1}$, $p<0.05$) over 1985–2012, coinciding with the global warming hiatus (Meehl et al., 2011; Kosaka and Xie, 2013). This trend results from the combined effects of the surface temperature change and the energy associated with the snowmelt. Compared with the land surface net energy flux observations from eddy covariance stations of FLUXNET, our estimated surface energy fluxes exhibit good consistency in seasonal variability. Turbulent energy fluxes from five datasets ($F_{LS1,}$ DEEPCv5, ERA5, ERA5-Land, MERRA2) show the overestimation compared with FLUXNET observations, partly due to the underestimation of the turbulent fluxes by the eddy covariance method (Wilson et al., 2002; Mauder et al., 2024). The turbulent fluxes inferred from F_{LS1} exhibit marginally better agreement with observations than reanalyses (Figure 6). However, the highest correlation coefficient between F_{LS1} and FLUXNET can reach 0.86, and the correlation coefficients of the anomaly time series are higher for F_{LS1} than for reanalysis data at approximately 71% of the observation sites. The spatial distribution of the net land surface energy flux uncertainty (STD) shows that the high discrepancies are concentrated in mid-to-high latitudes of the Northern Hemisphere and over the high-altitude areas. The STD in snow-covered regions (0.45 Wm^{-2}) is three times more than that in snow-free regions (0.13 Wm^{-2}), indicating the large uncertainty over snow-covered regions may be related to the poor representation of the energy consumed by the snowmelt in the land surface models.

Although ERA5 demonstrates significant improvements in forcing fields compared to ERA-Interim, its assimilation system still exhibits systematic energy balance deficiencies and insufficient representation of radiative forcing variations associated with natural aerosols (Soci et al., 2024, Allan and Merchant, 2025). The uncertainty in snowmelt affects the quality of our derived products and needs further investigation. Since the energy consumed by snowmelt can only be estimated from models rather than directly from observations, future advancements in satellite product of snowmelt and related variables are expected to improve current estimation. Further improvement in energy fluxes from the coming ERA6 can also be used to check the algorithm applied in this study.

In summary, our estimated land surface net energy flux generally outperforms existing reanalysis products in capturing interannual variability and local energy partitioning after comparison with station observations. It provides a robust foundation for diagnosing land–atmosphere coupling hotspots, evaluating energy budgets of next-generation land surface models, serving as an independent observational constraint in data assimilation, and investigating land heatwave mechanisms. This study has shown clearly the main uncertain regions in surface energy flux estimation, providing some information for the development and refinement of next-generation land surface models. This reconstructed land surface net energy fluxes can be combined with satellite-observed net surface radiative fluxes to generate the turbulent fluxes and investigate the systematic biases of other datasets, it will be used to update the DEEPC product following the procedures of Liu et al. (2017, 2020).

Acknowledgement

This work is jointly supported by the National Key Research and Development Program of China (2022YFF0802003); the National Natural Science Foundation of China (42275017, 42075036, 72293604, 42130605); the LASG key open project (20230273) from the Institute of Atmospheric Physics, Chinese Academy of Sciences, and the Postgraduate Education Innovation Project of Guangdong Ocean University (202523, 202144, 202253). Chunlei Liu is also supported by University of Reading as a visiting fellow. M. Mayer's efforts were supported by ESA contract ref. 4000145298/24/I-LR (MOTECUSOMA) and ESA Contract ref. 4000147586/I/25-LR. We acknowledge the modelling group who provide the LS3MIP and reanalysis data.

Data availability

The reconstructed data can be download from https://doi.org/10.57760/sciencedb.28002. The DEEPCv5 data are available at https://doi.org/10.17864/1947.000347, the CERES data can be download from https://ceres.larc.nasa.gov/Data/, the FLUXNET data can be accessed at https://FLUXNET.org/data/FLUXNET2015-dataset/, and the LS3IMIP land surface model simulations can be available from https://aims2.llnl.gov/search. ERA5 data can be available from https://cds.climate.copernicus.eu/datasets (accessed on 11 December 2024), and MERRA2 data can be downloaded from https://disc.gsfc.nasa.gov/ (accessed on 11 December 2024).

References

Allan, R. P., and C. J. Merchant, 2025: Reconciling Earth's growing energy imbalance with ocean warming. *Environmental Research Letters*, **20**(4), 044002, doi:10.1088/1748-9326/ad4a79.

Allan, R. P., C. Liu, N. G. Loeb, M. D. Palmer, M. Roberts, D. Smith, and P.-L. Vidale, 2014: Changes in global net radiative imbalance 1985–2012. *Geophys. Res. Lett.*, **41**, 5588–5597, doi:10.1002/2014GL060962.

Andrews, T., P. M. Forster, and J. M. Gregory, 2009: A surface energy perspective on climate change. *J. Climate*, **22**, 2557–2570, doi:10.1175/2008JCLI2759.1.

Bethke, I., Y. Wang, F. Counillon, et al., 2021: NorCPM1 and its contribution to CMIP6 DCPP. *Geosci. Model Dev.*, **14**, 7073–7116, doi:10.5194/gmd-14-7073-2021.

Bi, D., M. Dix, S. Marsland, et al., 2020: Configuration and spin-up of ACCESS-CM2, the new generation Australian Community Climate and Earth System Simulator Coupled Model. *J. South. Hemisphere Earth Syst. Sci.*, **70**, 225–251, doi:10.1071/ES19040.

Boer, G. J., 1993: Climate change and the regulation of the surface moisture and energy budgets. *Clim Dyn.*, **8**, 225–239, doi:10.1007/BF00198617.

Boucher, O., J. Servonnat, A. L. Albright, O. Aumont, Y. Balkanski, V. Bastrikov, et al., 2020: Presentation and evaluation of the IPSL-CM6A-LR climate model. *J. Adv. Model. Earth Syst.*, **12**, e2019MS002010, doi:10.1029/2019MS002010.

Boucher, O., S. Denvil, G. Levavasseur, et al., 2023: IPSL IPSL-CM6A-MR1 model output prepared for CMIP6 CMIP. Version 20231228. Earth System Grid Federation, doi:10.22033/ESGF/CMIP6.15922.

Burrows, S. M., M. Maltrud, X. Yang, Q. Zhu, N. Jeffery, X. Shi, et al., 2020: The DOE E3SM v1.1 biogeochemistry configuration: Description and simulated ecosystem-climate responses to historical changes in forcing. *J. Adv. Model. Earth Syst.*, **12**, e2019MS001766, doi:10.1029/2019MS001766.

Cheng, L., K. E. Trenberth, J. T. Fasullo, M. Mayer, M. Balmaseda, and J. Zhu, 2019: Evolution of ocean heat content related to ENSO. *J. Climate*, **32**, 3529−3556, doi:10.1175/JCLI-D-18-0607.1.

Chiodo, G., and L. Haimberger, 2010: Interannual changes in mass consistent energy budgets from ERA-Interim and satellite data. *J. Geophys. Res.*, **115**, D02112, doi:10.1029/2009JD012049.

Church, J. A., N. J. White, L. F. Konikow, C. M. Domingues, J. G. Cogley, E. Rignot, et al., 2011: Revisiting the Earth's sea-level and energy budgets from 1961 to 2008. *Geophys. Res. Lett.*, **38**, L18601, doi:10.1029/2011GL048794.

Church, J. A., P. U. Clark, A. Cazenave, et al., 2013: Sea level change. Climate Change 2013: The Physical Science Basis. Contribution of Working Group I to the Fifth Assessment Report of the Intergovernmental Panel on Climate Change*, T. F. Stocker et al., Eds., Cambridge University Press, 1137–1216.

Ciais, P., M. Reichstein, N. Viovy, et al., 2005: Europe-wide reduction in primary productivity caused by the heat and drought in 2003. *Nature*, **437**, 529–533, doi:10.1038/nature03972.

Cuesta-Valero, F. J., A. García-García, H. Beltrami, J. F. González-Rouco, and E. García-Bustamante, 2021: Long-term global ground heat flux and continental heat storage from geothermal data. *Clim.*

Past, **17**, 451–468, doi:10.5194/cp-17-451-2021.

Cuesta-Valero, F. J., et al., 2025: Robust increase in observed heat storage by the global subsurface. *Sci. Adv.*, **11**, eadw9958, doi:10.1126/sciadv.adw9958.

Danabasoglu, G., J.-F. Lamarque, J. Bacmeister, et al., 2020: The Community Earth System Model Version 2 (CESM2). *J. Adv. Model. Earth Syst.*, **12**, e2019MS001916, doi:10.1029/2019MS001916.

Döscher, R., M. Acosta, A. Alessandri, et al., 2022: The EC-Earth3 Earth system model for the Coupled Model Intercomparison Project 6. *Geosci. Model Dev.*, **15**, 2973–3020, doi:10.5194/gmd-15-2973-2022.

Douville, H., A. Quesada, S. I. Seneviratne, et al., 2016: Midlatitude daily summer temperatures reshaped by soil moisture under climate change. *Geophys. Res. Lett.*, **43**, 812–818, doi:10.1002/2015GL066222.

Fisher, J. B., K. P. Tu, and D. D. Baldocchi, 2008: Global estimates of the land–atmosphere water flux based on monthly AVHRR and ISLSCP-II data, validated at 16 FLUXNET sites. *Remote Sens. Environ.*, **112**, 901–919, doi:10.1016/j.rse.2007.06.025.

Gelaro, R., W. McCarty, M. J. Suárez, et al., 2017: The Modern-Era Retrospective Analysis for Research and Applications, version 2 (MERRA-2). *J. Climate*, **30**, 5419–5454, doi:10.1175/JCLI-D-16-0758.1.

Gentine, P., S. I. Seneviratne, H. Beltrami, E. Davin, R. Meier, A. García-García, and F. J. Cuesta-Valero, 2019: Large recent continental heat storage. *AGU Fall Meeting Abstracts*, GC51J-1078.

Gerken, T., B. L. Ruddell, R. Yu, et al., 2019: Robust observations of land-to-atmosphere feedbacks using the information flows of FLUXNET. *npj Clim. Atmos. Sci.*, **2**, 37, doi:10.1038/s41612-019-0094-4.

Golaz, J.-C., L. P. Van Roekel, X. Zheng, et al., 2022: The DOE E3SM Model version 2: Overview of the physical model and initial model evaluation. *J. Adv. Model. Earth Syst.*, **14**, e2022MS003156, doi:10.1029/2022MS003156.

Goswami, B. N., and J. Shukla, 1984: Quasi-periodic oscillations in a symmetric general circulation model. *J. Atmos. Sci.*, **41**, 20–37, doi:10.1175/1520-0469(1984)041<0020:QPOIAS>2.0.CO;2.

Gutjahr, O., D. Putrasahan, K. Lohmann, et al., 2019: Max Planck Institute Earth System Model (MPI-ESM1.2) for the High-Resolution Model Intercomparison Project (HighResMIP). *Geosci. Model Dev.*, **12**, 3241–3281, doi:10.5194/gmd-12-3241-2019.

Hakuba, M. Z., S. Fourest, T. Boyer, et al., 2024: Trends and variability in Earth's energy imbalance and ocean heat uptake since 2005. *Surv. Geophys.*, **45**, 1721–1756, doi:10.1007/s10712-024-09849-5.

Hakuba, M. Z., T. Frederikse, and F. W. Landerer, 2021: Earth's energy imbalance from the ocean perspective (2005–2019). *Geophys. Res. Lett.*, **48**, e2021GL093624, doi:10.1029/2021GL093624.

Harding, R., and Coauthors, 2011: WATCH: Current knowledge of the terrestrial global water cycle. *J. Hydrometeor.*, **12**, 1149–1156, doi:10.1175/JHM-D-11-024.1.

He, B., Q. Bao, X. Wang, et al., 2019: CAS FGOALS-f3-L Model Datasets for CMIP6 Historical Atmospheric Model Intercomparison Project Simulation. *Adv. Atmos. Sci.*, **36**, 771–778, doi:10.1007/s00376-019-9027-8.

Heimann, M., and M. Reichstein, 2008: Terrestrial ecosystem carbon dynamics and climate feedbacks. *Nature*, **451**, 289–292, doi:10.1038/nature06591.

Hersbach, H., B. Bell, P. Berrisford, et al., 2020: The ERA5 global reanalysis. *Quart. J. Roy. Meteor.*

Soc., **146**, 1999–2049, doi:10.1002/qj.3803.

Hipel, K. W., and A. I. Mcleod, 1994: *Time Series Modelling of Water Resources and Environmental Systems*. Elsevier, Amsterdam, 1012 pp.

Huntingford, C., P. M. Cox, P. D. L. Ritchie, et al., 2024: Acceleration of daily land temperature extremes and correlations with surface energy fluxes. *npj Clim. Atmos. Sci.*, **7**, 84, doi:10.1038/s41612-024-00626-0.

Hu, X., S. A. Sejas, M. Cai, et al., 2019: Decadal evolution of the surface energy budget during the fast warming and global warming hiatus periods in the ERA-interim. *Clim. Dyn.*, **52**, 2005–2016, doi:10.1007/s00382-018-4232-1.

Josey, S. A., S. Gulev, and L. Yu, 2013: Exchanges through the ocean surface. In *International Geophysics*, Vol. 103, Academic Press, 115–140, doi:10.1016/B978-0-12-391851-2.00005-2.

Kato, S., F. G. Rose, D. A. Rutan, et al., 2018: Surface irradiances of Edition 4.0 Clouds and the Earth's Radiant Energy System (CERES) Energy Balanced and Filled (EBAF) data product. *J. Climate*, **31**, 4501–4527, doi:10.1175/JCLI-D-17-0523.1.

Kikuchi, K., 2021: The boreal summer intraseasonal oscillation (BSISO): A review. *J. Meteor. Soc. Japan*, **99**, 933–972, doi:10.2151/jmsj.2021-045.

Kosaka, Y., and S. P. Xie, 2013: Recent global-warming hiatus tied to equatorial Pacific surface cooling. *Nature*, **501**, 403–407, doi:10.1038/nature12534.

Kouki, K., K. Luojus, A. Riihelä, et al., 2023: Evaluation of snow cover properties in ERA5 and ERA5-Land with several satellite-based datasets in the Northern Hemisphere in spring 1982–2018. *The Cryosphere Discussions*, **2023**, 1–33, doi:10.5194/tc-2023-86.

Levitus, S., J. I. Antonov, T. P. Boyer, et al., 2012: World ocean heat content and thermosteric sea level change (0–2000 m), 1955–2010. *Geophys. Res. Lett.*, **39**, L10603, doi:10.1029/2012GL051106.

Li, D., D. Folini, and M. Wild, 2023: Assessment of top of atmosphere, atmospheric and surface energy budgets in CMIP6 models on regional scales. *Earth Space Sci.*, **10**, e2022EA002758, doi:10.1029/2022EA002758.

Lin, Y., X. Huang, Y. Liang, et al., 2020: Community Integrated Earth System Model (CIESM): Description and evaluation. *J. Adv. Model. Earth Syst.*, **12**, e2019MS002036, doi:10.1029/2019MS002036.

Liu, C., and R. Allan, 2022: Reconstructions of the radiation fluxes at the top of atmosphere and net surface energy flux: DEEP-C Version 5.0. University of Reading, doi:10.17864/1947.000347.

Liu, C., R. P. Allan, P. Berrisford, et al., 2015: Combining satellite observations and reanalysis energy transports to estimate global net surface energy fluxes 1985–2012. *J. Geophys. Res. Atmos.*, **120**, 9374–9389, doi:10.1002/2015JD023264.

Liu, C., R. P. Allan, M. Mayer, et al., 2017: Evaluation of satellite and reanalysis-based global net surface energy flux and uncertainty estimates. *J. Geophys. Res. Atmos.*, **122**, 6250–6272, doi:10.1002/2017JD026616.

Liu, C., R. P. Allan, M. Mayer, et al., 2020: Variability in the global energy budget and transports 1985–2017. *Clim. Dyn.*, **55**, 3381–3396, doi:10.1007/s00382-020-05451-8.

Liu, C., Y. Yang, X. Liao, et al., 2022: Discrepancies in simulated ocean net surface heat fluxes over the North Atlantic. *Adv. Atmos. Sci.*, **39**, 1941–1955, doi:10.1007/s00376-022-1360-7.

Liu, C., L. Jin, N. Cao, et al., 2024: Assessment of the global ocean heat content and North Atlantic heat transport over 1993–2020. *npj Clim. Atmos. Sci.*, **7**, 314, doi:10.1038/s41612-024-00860-6.

Llovel, W., S. Purkey, B. Meyssignac, et al., 2019: Global ocean freshening, ocean mass increase and global mean sea level rise over 2005–2015. *Sci. Rep.*, **9**, 17717, doi:10.1038/s41598-019-54239-2.

Loeb, N. G., D. R. Doelling, H. Wang, et al., 2018: Clouds and the Earth's Radiant Energy System (CERES) Energy Balanced and Filled (EBAF) Top-of-Atmosphere (TOA) Edition-4.0 data product. *J. Climate*, **31**, 895–918, doi:10.1175/JCLI-D-17-0208.1.

Loeb, N. G., M. Mayer, S. Kato, et al., 2022: Evaluating twenty-year trends in Earth's energy flows from observations and reanalyses. *J. Geophys. Res. Atmos.*, **127**, e2022JD036686, doi:10.1029/2022JD036686.

Macdonald, A. M., and M. O. Baringer, 2013: Ocean heat transport. In *International Geophysics*, A. L. Gordon, H. R. Schmitt, and W. J. Emery, Eds., Vol. 103, Academic Press, 759–785, doi:10.1016/B978-0-12-391851-2.00029-5.

Majidi, F., S. Sabetghadam, M. Gharaylou, et al., 2025: Evaluation of the performance of ERA5, ERA5-Land and MERRA-2 reanalysis to estimate snow depth over a mountainous semi-arid region in Iran. *Journal of Hydrology: Regional Studies*, **58**, 102246, doi:10.1016/j.ejrh.2024.102246.

Mauder, M., M. Jung, P. Stoy, J. Nelson, and L. Wanner, 2024: Energy balance closure at FLUXNET sites revisited. Agricultural and Forest Meteorology, **358**, 110235, doi:10.1016/j.agrformet.2024.110235.

Mayer, J., M. Mayer, and L. Haimberger, 2021: Consistency and homogeneity of atmospheric energy, moisture, and mass budgets in ERA5. *J. Climate*, **34**(10), 3955−3974, doi:10.1175/JCLI-D-20-0676.1.

Mayer, J., M. Mayer, L. Haimberger, and C. Liu, 2022: Comparison of surface energy fluxes from global to local scale. *J. Climate*, **35**, 4551–4569, doi:10.1175/JCLI-D-21-0598.1.

Mayer, M., and L. Haimberger, 2012: Poleward atmospheric energy transports and their variability as evaluated from ECMWF reanalysis data. *J. Climate*, **25**, 734–752, doi:10.1175/JCLI-D-11-00202.1.

Mayer, M., L. Haimberger, J. M. Edwards, and P. Hyder, 2017: Toward consistent diagnostics of the coupled atmosphere and ocean energy budgets. *J. Climate*, **30**, 225−9246, doi:10.1175/JCLI-D-17-0137.1.

Mayer, M., S. Kato, M. Bosilovich, et al., 2024: Assessment of atmospheric and surface energy budgets using observation-based data products. *Surv. Geophys.*, **45**, 1827–1854, doi:10.1007/s10712-024-09827-x.

Meehl, G. A., J. M. Arblaster, J. T. Fasullo, A. S. Hu, and K. E. Trenberth, 2011: Model-based evidence of deep-ocean heat uptake during surface-temperature hiatus periods. *Nat. Clim. Change*, **1**, 360–364, doi:10.1038/nclimate1229.

Meyssignac, B., T. Boyer, Z. Zhao, et al., 2019: Measuring global ocean heat content to estimate the Earth energy imbalance. *Front. Mar. Sci.*, **6**, 432, doi:10.3389/fmars.2019.00432.

Mortimer, C., L. Mudryk, E. Cho, et al., 2024: Use of multiple reference data sources to cross-validate gridded snow water equivalent products over North America. *The Cryosphere*, **18**, 5619–5639, doi:10.5194/tc-18-5619-2024.

Muñoz-Sabater, J., E. Dutra, A. Agustí-Panareda, et al., 2021: ERA5-Land: A state-of-the-art global reanalysis dataset for land applications. *Earth Syst. Sci. Data*, **13**, 4349–4383, doi:10.5194/essd-13-4349-2021.

Pastorello, G., C. Trotta, E. Canfora, et al., 2020: The FLUXNET2015 dataset and the ONEFlux processing pipeline for eddy covariance data. *Sci. Data*, **7**, 225, doi:10.1038/s41597-020-0534-3.

Ren, Z., and T. Zhou, 2024: Understanding the alleviation of "Double-ITCZ" bias in CMIP6 models from the perspective of atmospheric energy balance. *Clim. Dyn.*, **62**, 6819–6839, doi:10.1007/s00382-024-07238-7.

Robledano, A., G. Picard, L. Arnaud, F. Larue, and I. Ollivier, 2022: Modelling surface temperature and radiation budget of snow-covered complex terrain. *The Cryosphere*, **16**, 559–579, doi:10.5194/tc-16-559-2022.

Schwartz, S. E., 2007: Heat capacity, time constant, and sensitivity of Earth's climate system. *J. Geophys. Res.*, **112**, D24S05, doi:10.1029/2007JD008746.

Schwing, F. B., T. Murphree, L. deWitt, and P. M. Green, 2002: The evolution of oceanic and atmospheric anomalies in the northeast Pacific during the El Niño and La Niña events of 1995–2001. *Prog. Oceanogr.*, **54**, 459–491, doi:10.1016/S0079-6611(02)00064-2.

Scoccimarro, E., A. Bellucci, and D. Peano, 2017: CMCC CMCC-CM2-HR4 model output prepared for CMIP6 HighResMIP hist-1950. Earth System Grid Federation [data set], doi:10.22033/ESGF/CMIP6.1359.

Séférian, R., P. Nabat, M. Michou, et al., 2019: Evaluation of CNRM Earth-System model, CNRM-ESM2-1: Role of Earth system processes in present-day and future climate. *J. Adv. Model. Earth Syst.*, **11**, 4182–4227, doi:10.1029/2019MS001791.

Seland, Ø., M. Bentsen, D. Olivié, et al., 2020: Overview of the Norwegian Earth System Model (NorESM2) and key climate response of CMIP6 DECK, historical, and scenario simulations. *Geosci. Model Dev.*, **13**, 6165–6200, doi:10.5194/gmd-13-6165-2020.

Seneviratne, S. I., D. Lüthi, M. Litschi, and C. Schär, 2006: Land-atmosphere coupling and climate change in Europe. *Nature*, **443**, 205–209, doi:10.1038/nature05095.

Seneviratne, S. I., T. Corti, E. L. Davin, et al., 2010: Investigating soil moisture–climate interactions in a changing climate: A review. *Earth-Sci. Rev.*, **99**, 125–161, doi:10.1016/j.earscirev.2010.02.004.

Senior, C. A., and Coauthors, 2016: Idealized climate change simulations with a high-resolution physical model: HadGEM3-GC2. *J. Adv. Model. Earth Syst.*, **8**, 813–830, doi:10.1002/2015MS000614.

Sheffield, J., G. Goteti, and E. F. Wood, 2006: Development of a 50-year high-resolution global dataset of meteorological forcings for land surface modeling. *J. Climate*, **19**, 3088–3111, doi:10.1175/JCLI3790.1.

Soci, C., H. Hersbach, A. Simmons, et al., 2024: The ERA5 global reanalysis from 1940 to 2022. *Quart. J. Roy. Meteor. Soc.*, **150**, 4014–4048, doi:10.1002/qj.4803.

Stephens, G. L., J. Li, M. Wild, et al., 2012: An update on Earth's energy balance in light of the latest global observations. *Nat. Geosci.*, **5**, 691–696, doi:10.1038/ngeo1580.

Swart, N. C., J. N. S. Cole, V. V. Kharin, et al., 2019: The Canadian Earth System Model version 5 (CanESM5.0.3). *Geosci. Model Dev.*, **12**, 4823–4873, doi:10.5194/gmd-12-4823-2019.

Tatebe, H., T. Ogura, T. Nitta, et al., 2019: Description and basic evaluation of simulated mean state, internal variability, and climate sensitivity in MIROC6. *Geosci. Model Dev.*, **12**, 2727–2765, doi:10.5194/gmd-12-2727-2019.

Tian, Y., A. Kleidon, C. Lesk, et al., 2024: Characterizing heatwaves based on land surface energy budget. *Commun. Earth Environ.*, **5**, 617, doi:10.1038/s43247-024-01784-y.

Trenberth, K. E., and A. Solomon, 1994: The global heat balance: Heat transports in the atmosphere and ocean. *Clim. Dyn.*, **10**, 107–134, doi:10.1007/BF00210625.

Trenberth, K. E., and J. T. Fasullo, 2017: Atlantic meridional heat transports computed from balancing Earth's energy locally. *Geophys. Res. Lett.*, **44**, 1919–1927, doi:10.1002/2016GL072475.

Trenberth, K. E., J. M. Caron, and D. P. Stepaniak, 2001: The atmospheric energy budget and implications for surface fluxes and ocean heat transports. *Clim. Dyn.*, **17**, 259–276, doi:10.1007/PL00007927.

Trenberth, K. E., Y. Zhang, J. T. Fasullo, and L. Cheng, 2019: Observation-based estimates of global and basin ocean meridional heat transport time series. *J. Climate*, **32**, 4567–4583, doi:10.1175/JCLI-D-18-0872.1.

Trenberth, K. E., J. T. Fasullo, and J. Kiehl, 2009: Earth's global energy budget. *Bull. Amer. Meteor. Soc.*, **90**, 311−323, doi:10.1175/2008BAMS2634.1.

Urraca, R., and N. Gobron, 2023: Temporal stability of long-term satellite and reanalysis products to monitor snow cover trends. The Cryosphere, **17**(3), 1023−1052, doi: 10.5194/tc-17-1023-2023.

Valdivieso, M., K. Haines, M. Balmaseda, et al., 2017: An assessment of air–sea heat fluxes from ocean and coupled reanalyses. *Clim. Dyn.*, **49**, 983–1008, doi:10.1007/s00382-015-2843-3.

Van Den Hurk, B., H. Kim, G. Krinner, et al., 2016: LS3MIP (v1.0) contribution to CMIP6: The Land Surface, Snow and Soil moisture Model Intercomparison Project – aims, setup and expected outcome. *Geosci. Model Dev.*, **9**, 2809–2832, doi:10.5194/gmd-9-2809-2016.

Viovy, N., and P. Ciais, 2009: A combined dataset for ecosystem modelling. Available online at: http://esgf.extra.cea.fr/thredds/catalog/store/p529viov/cruncep/catalog.html.

Volodin, E. M., E. V. Mortikov, S. V. Kostrykin, et al., 2017: Simulation of the Present-day Climate with the Climate Model INMCM5. *Clim Dyn.*, **49**, 3711–3734, doi:10.1007/s00382-017-3539-7.

Voldoire, A., D. Saint-Martin, S. Sénési, et al., 2019: Evaluation of CMIP6 DECK experiments with CNRM-CM6-1. *J. Adv. Model. Earth Syst.*, **11**, 2177–2213, doi:10.1029/2019MS001683.

von Schuckmann, K., M. D. Palmer, K. E. Trenberth, et al., 2016: An imperative to monitor Earth's energy imbalance. *Nat. Clim. Change*, **6**, 138–144, doi:10.1038/nclimate2876.

Wang, R., J. Lu, P. Gentine, and H. Chen, 2024: Global pattern of soil temperature exceeding air temperature and its linkages with surface energy fluxes. *Environ. Res. Lett.*, **19**, 104029, doi:10.1088/1748-9326/ad7279.

Weedon, G. P., S. Gomes, P. Viterbo, et al., 2011: Creation of the WATCH forcing data and its use to assess global and regional reference crop evaporation over land during the twentieth century. *J. Hydrometeor.*, **12**, 823–848, doi:10.1175/2011JHM1369.1.

Wild, M., and M. G. Bosilovich, 2024: The global energy balance as represented in atmospheric reanalyses. *Surv. Geophys.*, **45**, 1799–1825, doi:10.1007/s10712-024-09861-9.

Wild, M., 2017: Towards global estimates of the surface energy budget. *Curr. Clim. Change Rep.*, **3**, 87–97, doi:10.1007/s40641-017-0058-x.

Wild, M., 2020: The global energy balance as represented in CMIP6 climate models. *Clim Dyn.*, **55**, 553−577, doi:10.1007/s00382-020-05282-7.

Williams, K. D., C. M. Harris, A. Bodas-Salcedo, et al., 2015: The Met Office Global Coupled model 2.0 (GC2) configuration. *Geosci. Model Dev.*, **8**, 1509–1524, doi:10.5194/gmd-8-1509-2015.

Wilson, K., A. Goldstein, E. Falge, et al., 2002: Energy balance closure at FLUXNET sites. Agricultural and Forest Meteorology, **113**, 223−243, doi:10.1016/S0168-1923(02)00109-0.

Winkelbauer, S., M. Mayer, V. Seitner, E. Zsoter, H. Zuo, and L. Haimberger, et al., 2022: Diagnostic evaluation of river discharge into the Arctic Ocean and its impact on oceanic volume transports. *Hydrol. Earth Syst. Sci.*, **26**(2), 279–304, doi:10.5194/hess-26-279-2022.

World Meteorological Organization, 1997: WMO Statement on the Status of the Global Climate in 1996. WMO, Geneva, 11 pp.

Wu, T., R. Yu, Y. Lu, et al., 2021: BCC-CSM2-HR: a high-resolution version of the Beijing Climate Center Climate System Model. *Geosci. Model Dev.*, **14**, 2977–3006, doi:10.5194/gmd-14-2977-2021.

Xu, T., A. Zhang, X. Xu, and G. Jia, 2023: Synchronized slowdown of climate warming and carbon sink enhancement over deciduous broadleaf forests based on FLUXNET analysis. *Ecol. Indic.*, **155**, 111042, doi:10.1016/j.ecolind.2023.111042.

Yukimoto, S., H. Kawai, T. Koshiro, et al., 2019: The Meteorological Research Institute Earth System Model version 2.0, MRI-ESM2.0: Description and basic evaluation of the physical component. *J. Meteorol. Soc. Japan*, **97**, 931–965, doi:10.2151/jmsj.2019-051.

Zemp, M., M. Huss, E. Thibert, et al., 2019: Global glacier mass changes and their contributions to sea-level rise from 1961 to 2016. *Nature*, **568**, 382–386, doi:10.1038/s41586-019-1071-0.

Zhang, H., M. Zhang, J. Jin, et al., 2020: CAS-ESM 2: Description and climate simulation performance of the Chinese Academy of Sciences (CAS) Earth System Model (ESM) version 2. *J. Adv. Model. Earth Syst.*, **12**, e2020MS002210, doi:10.1029/2020MS002210.

Zhang, X., Y. Dai, H. Cui, J. He, and G. Wang, 2017: Evaluating common land model energy fluxes using FLUXNET data. *Adv. Atmos. Sci.*, **34**, 1035–1046, doi:10.1007/s00376-017-6251-y.

Electronic Supplementary Material

Table S1. FUXNET sites description

Site	Lat	Lon	Period (in this study)	Fs	Turbulent fluxes
AT-Neu	47.11667°N	11.3175°E	2002-2012	✓	✓
AU-ASM	22.28°S	133.25°W	2010-2014	✓	✓
AU-DaP	14.0633°S	131.3181°E	2007-2013	✓	✓
AU-Das	14.16°S	131.39°W	2009-2014	✓	✓
AU-Dry	15.2588°S	132.3706°E	2008-2014		✓
BE-Bra	51.30761°N	4.51984°E	2001-2014	✓	✓
BE-Vie	50.30493°N	5.99812°E	2001-2014		✓
CA-Gro	48.2167°N	82.1156°W	2004-2014	✓	✓
CA-Man	55.87962°N	98.48081°W	2000-2008	✓	✓
CA-Oas	53.62889°N	106.19779°W	2001-2010		✓
CA-Qfo	49.6925°N	74.34206°W	2003-2010	✓	✓
CA-SF3	54.09156°N	106.00526°W	2001-2006	✓	✓
CA-TP1	42.66093611°N	80.55951944°W	2002-2014	✓	✓
CA-TP4	42.71°N	80.36°W	2003-2006	✓	✓
CH-Dav	46.81553°N	9.85591°E	1997-2014	✓	✓
CH-Fru	47.11583°N	8.53778°E	2006-2014	✓	✓
CH-Oe2	47.28642°N	7.73375°E	2005-2014		✓
CN-Cng	44.5934°N	123.5092°E	2007-2010		✓
CZ-BK1	49.50208°N	18.53688°E	2004-2014		✓
CZ-wet	49.02465°N	14.77035°E	2007-2014	✓	✓
DE-Geb	51.10°N	10.91463°E	2002-2014	✓	✓
DE-Kli	50.89306°N	13.52238°E	2004-2014	✓	✓
DE-Lnf	51.32822°N	10.3678°E	2003-2012		✓
DE-Tha	50.96°N	13.56515°E	2005-2014	✓	✓
ES-LJu	36.92659°N	2.75212°W	2004-2013	✓	✓
FI-Hyy	61.84741°N	24.29477°E	1999-2014	✓	✓
FI-Sod	67.36239°N	26.63859°E	2001-2014		✓
FR-Fon	48.47636°N	2.7801°E	2006-2014	✓	✓
FR-Gri	48.84422°N	1.95191°E	2004-2014	✓	✓
FR-Pue	43.74°N	3.5957°E	2006-2011	✓	✓
GH-Ank	5.26854°N	2.69421°W	2012-2014		✓
GL-NuF	64.13083°N	51.38611°W	2009-2014		✓
GL-ZaH	74.47328°N	20.5503°W	2001-2014	✓	✓
IT-Bci	40.52375°N	14.95744°E	2004-2014		✓
IT-Lav	45.96°N	11.28132°E	2003-2008	✓	✓
IT-MBo	46.01468°N	11.04583°E	2003-2014	✓	✓
IT-Ren	46.58686°N	11.43369°E	2001-2013	✓	✓
IT-Sro	43.72786°N	10.28444°E	2001-2012	✓	✓
JP-SMF	35.2617°N	137.0788°E	2003-2006		✓

Site	Lat	Lon	Period (in this study)	Fs	Turbulent fluxes
MY-PSO	2.973°N	102.3062°E	2003-2009		✓
NL-Loo	52.17°N	5.74356°E	2002-2014	✓	✓
RU-Cok	70.82941°N	147.49428°E	2003-2014		✓
US-Blo	38.8953°N	120.6328°W	1999-2007	✓	✓
US-GBT	41.36579°N	106.2397°W	2001-2006	✓	✓
US-GLE	41.37°N	106.24°W	2006-2014	✓	✓
US-Ha1	42.5378°N	72.1715°W	1997-2012	✓	✓
US-IB2	41.84062°N	88.24103°W	2005-2011	✓	✓
US-Los	46.0827°N	89.9792°W	2001-2014	✓	✓
US-Me2	44.4523°N	121.5574°W	2002-2014	✓	✓
US-MMS	39.32°N	86.41°W	2003-2014	✓	✓
US-NR1	40.03°N	105.55°W	2008-2014	✓	✓
US-Oho	41.5545°N	83.8438°W	2005-2013		✓
US-PFa	45.9459°N	90.2723°W	2001-2014		✓
US-SRC	31.9083°N	110.8395°W	2009-2014		✓
US-SRG	31.789379°N	110.827675°W	2009-2014		✓
US-SRM	31.8214°N	110.8661°W	2005-2014	✓	✓
US-Syv	46.242°N	89.3477°W	2001-2014		✓
US-Var	38.41°N	120.95°W	2009-2013		✓
US-WCr	45.8059°N	90.0799°W	2001-2014		✓
US-Whs	31.7438°N	110.0522°W	2007-2014	✓	✓

AT: Austria; AU: Australia; BE: Belgium; CA: Canada; CH: Switzerland; CN: China; CZ: Czech Republic; DE: Germany; ES: Spain; FI: Finland; FR: France; GH: Ghana; GL: Greenland; IT: Italy; JP: Japan; MY: Malaysia; NL: Netherlands; RU: Russia; US: USA;

Table S2. Eighteen AMIP6 models and brief descriptions

Dataset	Period (in this study)	Resolution	Reference
ACCESS-CM2		1.25°×1.875°	Bi et al. (2020)
BCC-CSM2-MR		1.25°×1.875°	Wu et al. (2021)
CanESM5		2.81°×2.81°	Swart et al. (2019)
CAS-ESM2-0		1.417°×1.406°	Zhang et al. (2020)
CESM2		0.94°×1.25°	Danabasoglu et al. (2020)
CIESM		0.94°×1.25°	Lin et al. (2020)
CMCC-CM2-HR4		0.94°×1.25°	Scoccimarro et al. (2017)
E3SM-2-0		1.0°×1.0°	Golaz et al. (2022)
EC-Earth3	1985-2014	0.7°×0.7°	Döscher et al., (2022)
FGOALS-f3-L		1.0°×1.25°	He et al. (2019)
INM-CM5-0		1.5°×2.0°	Volodin et al. (2017)
IPSL-CM6A-MR1		0.7°×1.4°	Boucher et al. (2023)
IPSL-CM6A-LR		1.26°×2.5°	Boucher et al. (2020)
MIROC6		1.41°×1.41°	Tatebe et al. (2019)
MPI-ESM1-2-HR		0.94°×0.94°	Gutjahr et al. (2019)
MRI-ESM2-0		1.125°×1.125°	Yukimoto et al. (2019)
NorCPM1		1.895°×2.5°	Bethke et al. (2021)
NorESM2-LM		1.895°×2.5°	Seland et al. (2020)

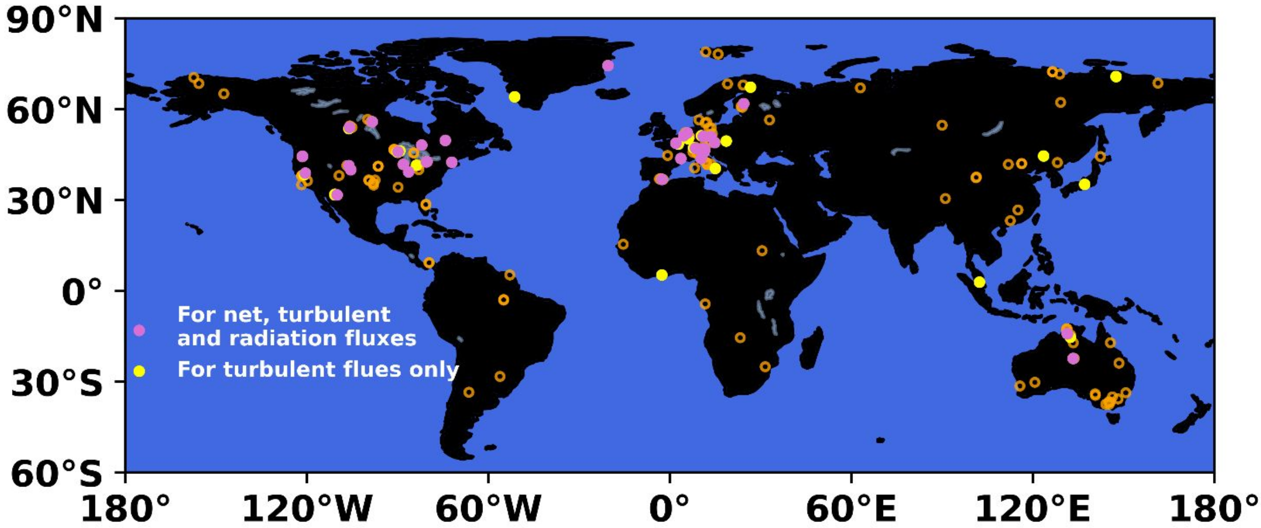

Figure S1. Circles represent locations of observation sites, and the data from solid circle sites are used in this study.

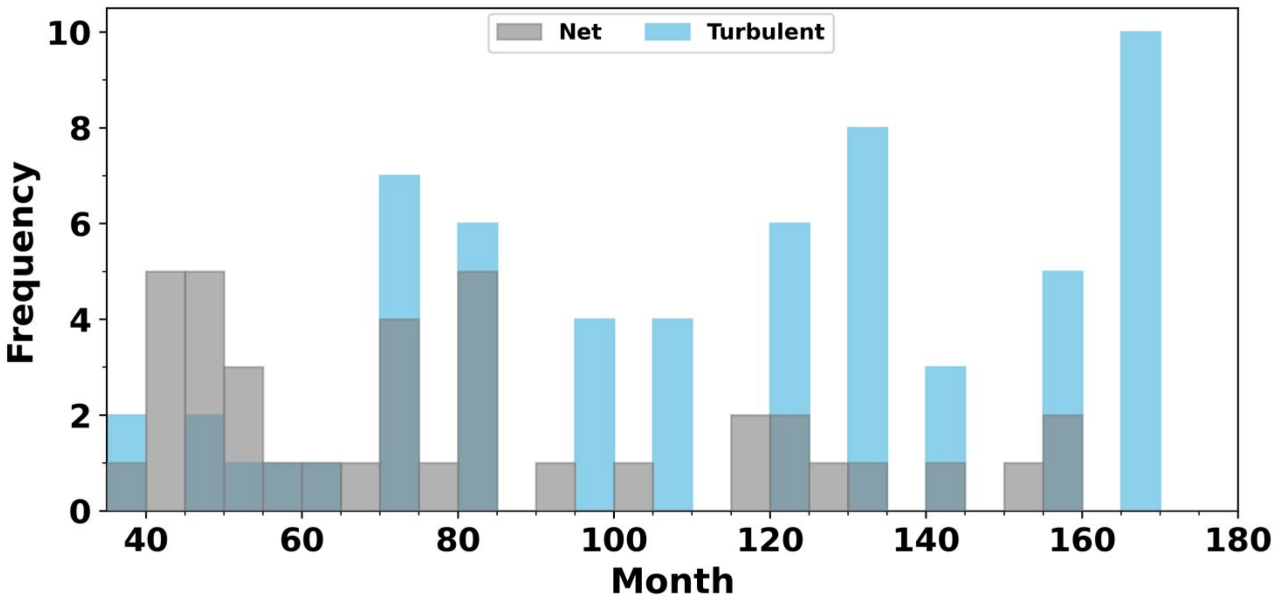

Figure S2. Station frequency of the FLUXNET data. The x-axis is the length of the data at a station and the bin size is 5 months.

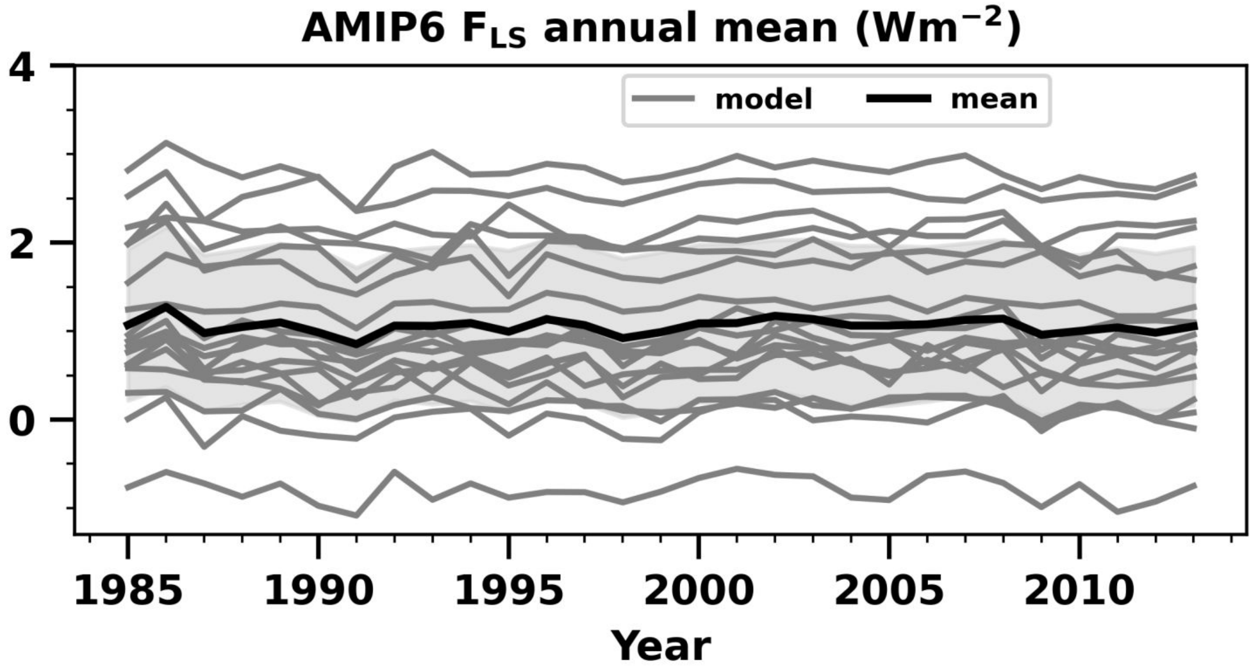

Figure S3. Time series of the annual mean net surface energy fluxes from 18 AMIP6 model simulations as listed in Table S2. The solid black line is the ensemble mean and the gray shading is the mean ± one standard deviation from 19 lines.

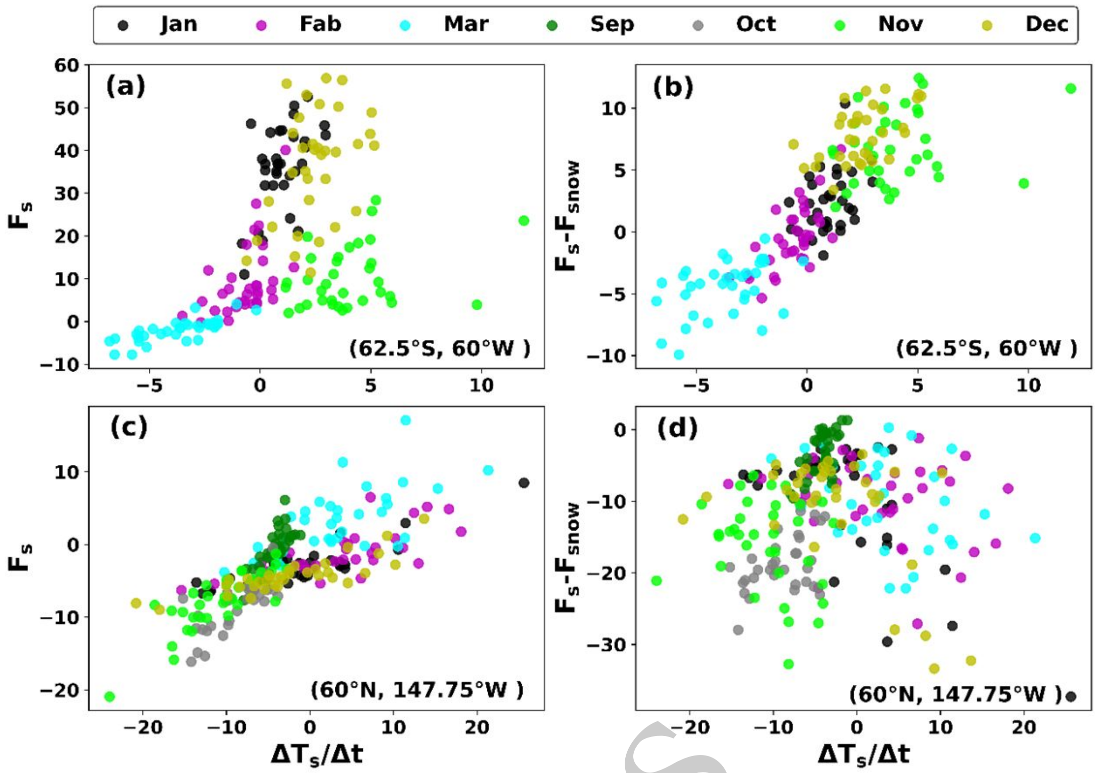

Figure S4. Scatter plots of the relationship between the net surface energy flux and temperature change at grid points (a-b) (62.5°S, 60°W) and (c-d) (60°N, 147.8°W), with (right column) and without (left column) snowmelt considerations.

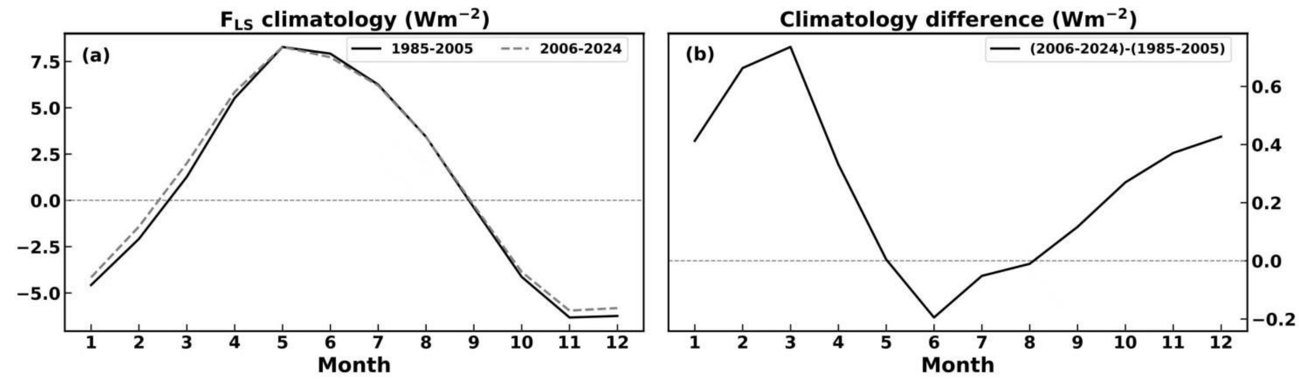

Figure S5. (a) Net surface energy flux climatology over 1985-2005 and 2006-2024, (b) climatology difference (2006-2024 minus 1985-2005).

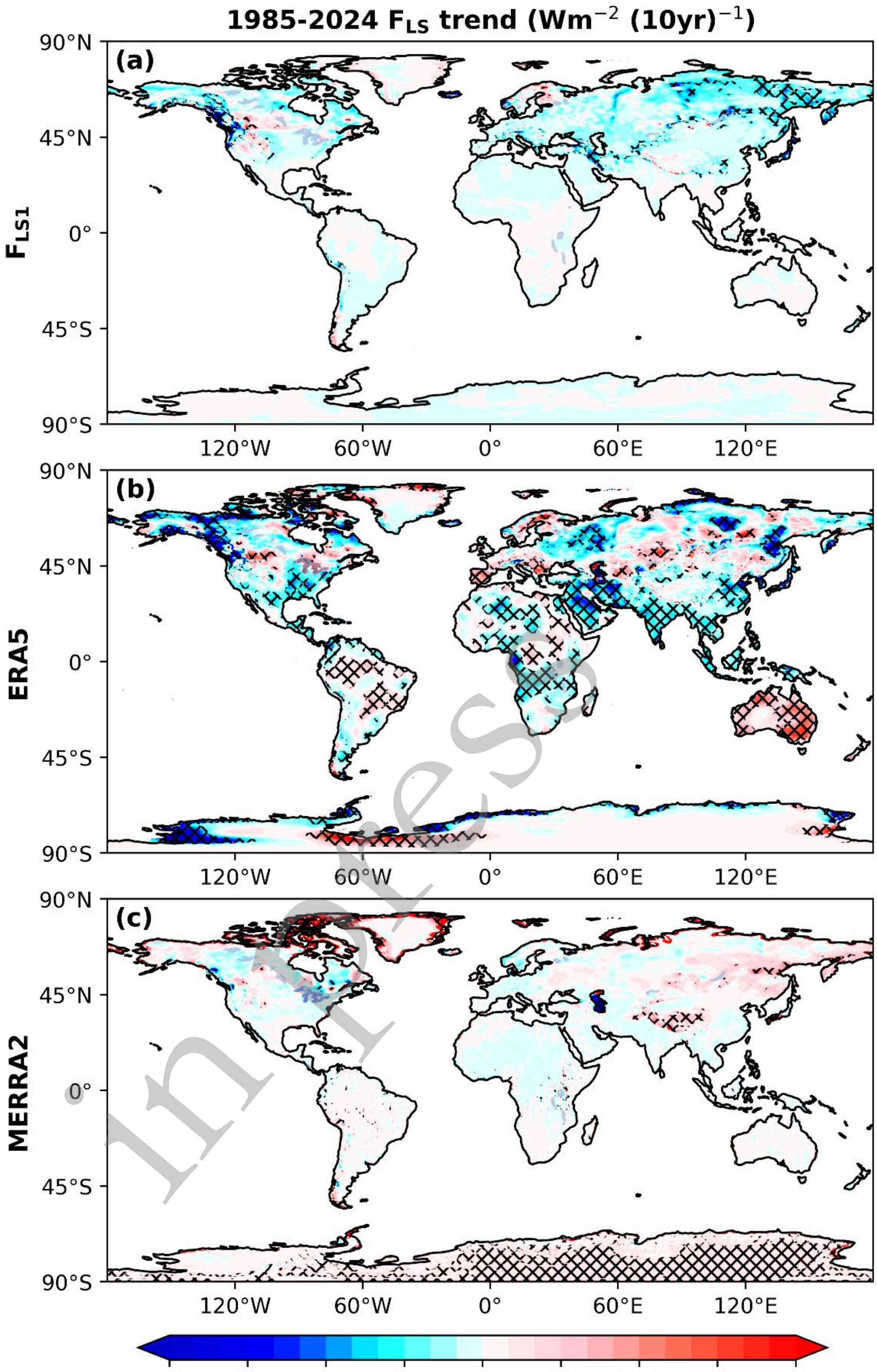

Figure S6. Spatial distribution of F_{LS} trends over 1985-2024 for (a) F_{LS1}, (b) ERA5, and (c) MERRA2. The grids with crosses indicate the trends are statistically significant ($p < 0.05$).

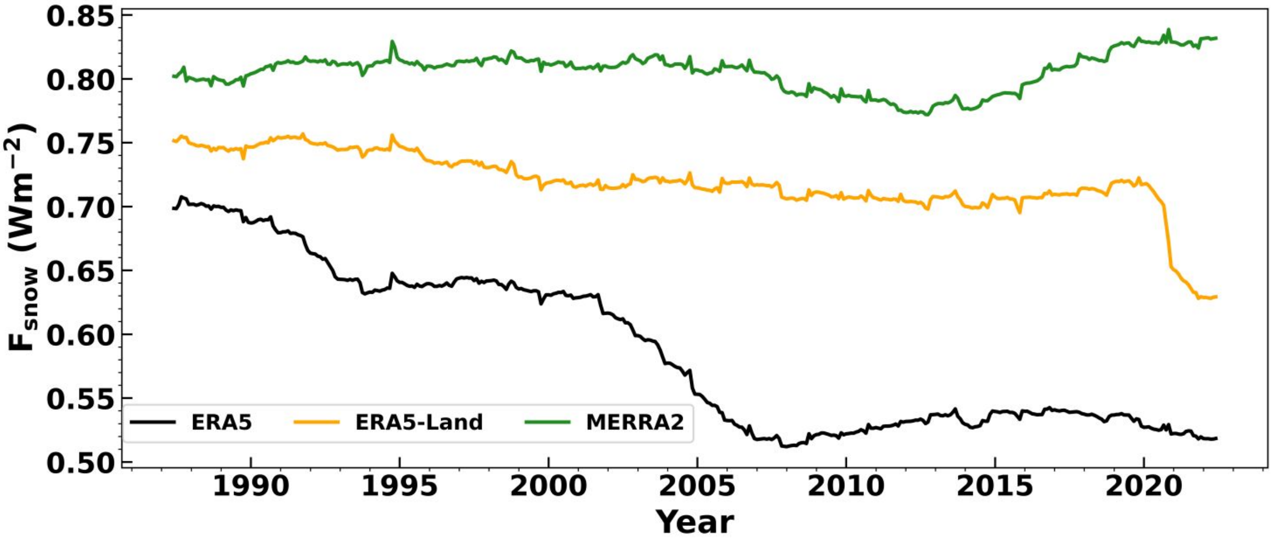

Figure S7. Time series of the F_{snow} from ERA5, ERA5-Land and MERRA2. All lines have been smoothed by 60 month running mean.

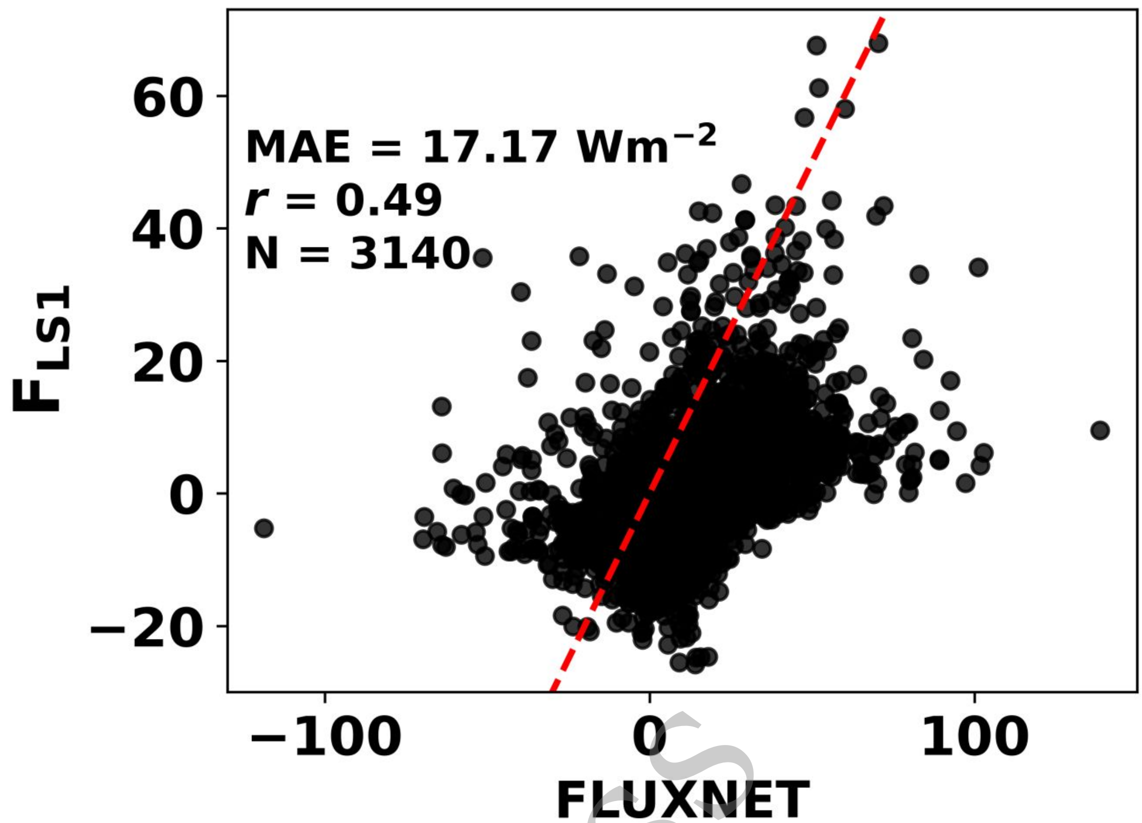

Figure S8. Scatter plot of net surface energy fluxes between F_{LS1} and FLUXNET. The dashed red line is the symmetrical line y=x, ***r*** is the correlation coefficient and N is the total number of data points.

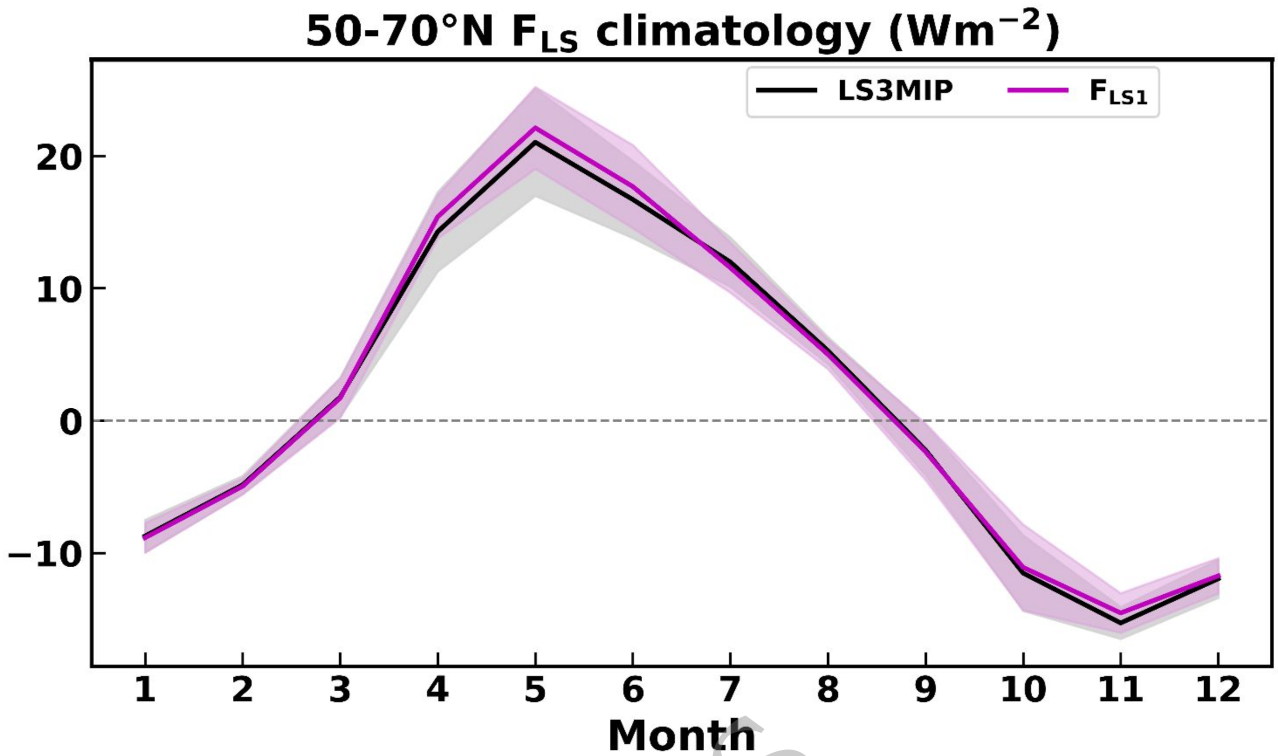

Figure S9. Seasonal cycle of F_{LS} over the 50–70°N region during the period 1985–2012.